

# SPATIO-TEMPORAL LOCAL INTERPOLATION OF GLOBAL OCEAN HEAT TRANSPORT USING ARGO FLOATS: A DEBIASED LATENT GAUSSIAN PROCESS APPROACH

BY BEOMJO PARK<sup>1,\*</sup>, MIKAEL KUUSELA<sup>1,†</sup>, DONATA GIGLIO<sup>2</sup> AND ALISON GRAY<sup>3</sup>

<sup>1</sup>*Dept. of Statistics & Data Science, Carnegie Mellon University, [\\*beomjo@stat.cmu.edu](mailto:beomjo@stat.cmu.edu); [†mkuusela@andrew.cmu.edu](mailto:mkuusela@andrew.cmu.edu)*

<sup>2</sup>*Dept. of Atmospheric and Oceanic Sciences, University of Colorado Boulder, [donata.giglio@colorado.edu](mailto:donata.giglio@colorado.edu)*

<sup>3</sup>*School of Oceanography, University of Washington, [argray@uw.edu](mailto:argray@uw.edu)*

The world ocean plays a key role in redistributing heat in the climate system and hence in regulating Earth’s climate. Yet statistical analysis of ocean heat transport suffers from partially incomplete large-scale data intertwined with complex spatio-temporal dynamics, as well as from potential model misspecification. We present a comprehensive spatio-temporal statistical framework tailored to interpolating the global ocean heat transport using in-situ Argo profiling float measurements. We formalize the statistical challenges using latent local Gaussian process regression accompanied by a two-stage fitting procedure. We introduce an approximate Expectation-Maximization algorithm to jointly estimate both the mean field and the covariance parameters, and refine the potentially under-specified mean field model with a debiasing procedure. This approach provides data-driven global ocean heat transport fields that vary in both space and time and can provide insights into crucial dynamical phenomena, such as El Niño & La Niña, as well as the global climatological mean heat transport field, which by itself is of scientific interest. The proposed framework and the Argo-based estimates are thoroughly validated with state-of-the-art multimission satellite products and shown to yield realistic subsurface ocean heat transport estimates.

**1. Introduction.** The ocean plays a pivotal role in regulating Earth’s climate on regional to global scales (e.g., [Bryden and Imawaki, 2001](#); [Macdonald and Baringer, 2013](#); [Stocker, 2013](#)). Notably, it redistributes the excess heat taken up at the equator, transporting it to higher latitudes where it is released to the atmosphere ([Trenberth and Solomon, 1994](#); [Ganachaud and Wunsch, 2000](#); [Trenberth and Caron, 2001](#); [Forget and Ferreira, 2019](#)). Convergence and divergence of heat in the ocean also have impacts on regional sea level (via thermal expansion of sea water, e.g., [Forget and Ponte \(2015\)](#)), with implications for local populations. Ocean heat transport can additionally regulate regional temperature extremes in the ocean, with implications for marine ecosystems. As an example of the latter, [Behrens, Fernandez and Sutton \(2019\)](#) describe a causal link between ocean heat content and the area and intensity of marine heatwaves in the Tasman Sea: ocean heat content fluctuations in the Tasman Sea are largely controlled by meridional transport of heat in the ocean; hence, better estimates of ocean heat transport can help improve forecasts of marine heatwaves, with potential implications for the management of ecosystems in Australasia. Obtaining an accurate picture of the heat transport within and across ocean basins is therefore critical to understanding changes in the climate system and for data-driven policy and decision making in a changing climate.

In this paper, we present a statistical framework to characterize ocean heat transport (OHT) over the global ice-free ocean during 2007-2018, based on direct observations of temperature

---

*Keywords and phrases:* latent Gaussian process regression, local kriging, approximate EM, model misspecification, physical oceanography.

and salinity in the upper 2000 m of the ocean. Historically, global OHT has been estimated indirectly by subtracting the atmospheric component from total heat transport estimates (Trenberth and Solomon, 1994; Trenberth and Caron, 2001), leveraging top-of-the-atmosphere radiation measurements from satellites. Direct OHT estimates are typically made at only a few locations where suitable ship- or mooring-based observations are available and thus do not provide a global view. The Argo array of profiling floats, in contrast, collects observations of temperature and salinity in the upper 2000 m of the open ocean with unprecedented spatio-temporal coverage (Jayne et al., 2017). These data provide an extraordinary opportunity to quantify, on a global scale, the spatial and temporal variability of upper ocean heat transport.

When Argo measurements are used in scientific analyses, a vast majority of literature relies on spatio-temporally interpolated temperature and salinity maps that convert the Argo measurements sampled irregularly in space and time to a regular spatio-temporal grid (e.g. Roemmich and Gilson, 2009; Good, Martin and Rayner, 2013). However, unlike temperature and salinity, interpolating OHT faces a critical challenge from the fact that OHT—a vertical integral of essentially the product between temperature and velocity—is only partially observed by common oceanographic instruments, including Argo floats. Even though each float records temperature directly, the velocity, and thus OHT, is not directly measured (and can not be derived from a single observation) but rather has to be inferred as the gradient of a variable computed from the in-situ observations. Such latent construction constitutes the crux of a statistical challenge distinct from archetypal spatio-temporal interpolation problems.

The latent nature of the problem is intertwined with the classical challenges in modern large-scale spatio-temporal statistics: spatio-temporal local dependency, global heterogeneity, and model misspecification, not to mention the large volume of in-situ Argo data (see e.g., Cressie and Wikle, 2011). In particular, (1) both the latent velocity field and the OHT field are globally non-stationary spatio-temporal processes; (2) sharp ocean fronts are insufficiently identified when model misspecification is not properly addressed; (3) the massive number of irregularly-spaced, sparse spatio-temporal observations demands computationally efficient methods that are able to account for both the variability and the underlying spatio-temporal structure of the data.

To overcome these challenges, we propose a two-stage statistical framework based on de-biased local Gaussian process regression (LGPR), extending the work of Kuusela and Stein (2018a) on Argo temperature fields. The framework is a comprehensive suite of statistical techniques tailored to OHT interpolation, in that we formalize the statistical challenges into a latent LGPR model accompanied by a two-stage fitting procedure, introduce an approximate Expectation-Maximization (EM) algorithm (Dempster, Laird and Rubin, 1977) to jointly estimate both the mean field and the covariance parameters, and refine the potentially misspecified model with a debiasing procedure. The two-stage procedure solves the spatio-temporally correlated latent variable problem by predicting the latent velocity fields on the first stage using LGPR with a related oceanographic variable whose realizations are directly measured for each Argo profile. Conditional on the predicted velocity at the observed spatio-temporal coordinates of the Argo profiles, we then interpolate OHT on the second stage over the entire global ocean during years 2007 to 2018 again using LGPR. Our approach is unifying since the same LGPR framework succinctly represents both velocity and OHT fields.

We improve the LGPR approach of Kuusela and Stein (2018a) by simultaneously estimating both the mean field and the covariance parameters with an iterative EM algorithm in a computationally efficient manner. Kuusela and Stein (2018a) focus on estimating a local space-time covariance model from mean-centered temperature observations where the mean field was estimated with ordinary least squares (OLS). Joint estimation on both mean and covariance parameters is imperative in OHT estimation, as we need to estimate the actual mean field of the latent process not only the mean-centered field. Joint estimation of both

mean and the covariance parameters is not uncommon in spatial statistics. For instance, the sub-optimality of OLS in a regression kriging context is typically resolved using generalized least squares (GLS), which accounts for the spatio-temporal correlation of the residuals (Cressie, 1993). A similar iterative GLS approach was also adopted to estimate velocities from Argo data in Gray and Riser (2015). Our approximate EM algorithm shares the same spirit but requires a separate treatment since the LGPR model localizes the spatio-temporal covariances seasonally along the temporal axis within the span of the spatio-temporal mean.

Predicting the latent velocity field with an under-specified model may result in a concerning bias. It is vital to correct the bias since a bias in the latent field would propagate to the second stage, degrading the final OHT interpolation. By formalizing an approach previously used by oceanographers (Roemmich and Gilson, 2009), we provide an intuitive debiasing procedure by estimating the bias from the predicted field and then subtracting the estimated bias in an iterative manner. This data-driven debiasing procedure is shown to capture sharper ocean fronts bearing crucial importance in ocean dynamics and to improve prediction and interpolation, as confirmed by a validation study based on satellite data. While our approach has close connections to iterative bias-correction in classical regression modeling (Kuk, 1995; Guerrier et al., 2020) and to accounting for model discrepancy in Bayesian computer model calibration (Kennedy and O’Hagan, 2001; Bayarri et al., 2007; Brynjarsdóttir and O’Hagan, 2014), it has, to the best of our knowledge, not been previously embraced by the spatio-temporal statistics community.

Our work aligns with the oceanographic community’s interests yet does not address all of the challenges in characterizing global OHT with in-situ Argo measurements. Currently, the Argo fleet does not fully resolve the narrow western boundary currents that are a key component of the global OHT, nor does it sample below 2000 m on a global scale (although expansions of the array to address both of these deficiencies are being planned). In addition, the portion of the velocity field directly driven by the winds (i.e., the Ekman velocity) cannot be estimated from measurements of temperature and salinity, despite playing a non-negligible role in OHT. Thus, Argo observations must be integrated with other datasets for full-depth, cross-basin estimates of OHT. Even though our paper focuses only on Argo-based OHT estimates, in Section H of the Supplementary Material (Park et al., 2020), we provide improved estimates in the western North Atlantic Ocean by applying our proposed framework to data from both Argo floats and Spray gliders (Rudnick, Davis and Sherman, 2016). An alternative approach for estimating OHT from Argo observations (Verdière, Meunier and Ollitrault, 2019) contends with these issues by combining float- and ship-based datasets. That method, however, entails solving two Poisson equations over the entire domain, and thus the results depend heavily on the adhoc specification of accurate boundary conditions.

The rest of the paper is organized as follows. Section 2 defines ocean heat transport and gives a brief overview of the related scientific context and the Argo dataset. In Section 3, we present the complete framework for quantifying global ocean heat transport fields based on Argo data. This includes the spatio-temporal model specification, estimation, and refinement procedures. Section 4 presents the estimated latent velocity and OHT fields and illustrates a scientific application of the resulting OHT estimates in the context of the El Niño–Southern Oscillation. Section 5 validates both our proposed method and the resulting estimates using state-of-the-art satellite products. Section 6 discusses the results and implications along with future research directions. Our code is publicly available online at [https://github.com/beomjopark/OHT\\_analysis](https://github.com/beomjopark/OHT_analysis) for reproducibility and reuse of the proposed framework.

**2. Scientific Background and Data.** Before describing our statistical methodology, we provide a brief introduction to the computation of OHT, as well as relevant details of the

Argo profiling float dataset. The reader is referred to [Macdonald and Baringer \(2013\)](#) for a detailed review of OHT and its impact in the climate system and to [Wong et al. \(2020\)](#) for a thorough treatment of the Argo dataset.

Fundamentally, the ocean transports heat because it moves water with velocity  $\mathbf{v}$  while containing an amount of heat proportional to its potential temperature  $\theta$  (where  $\theta$  removes the thermodynamic effect of pressure from the in-situ temperature  $T$ ). This heat flux can be integrated vertically at any location in the ocean to produce an estimate of OHT. We thus define OHT at a given spatial coordinate  $\mathbf{x} = (x, y) \in \mathbb{X} \subseteq \mathbb{R}^2$  and temporal coordinate  $t \in \mathbb{T} \subseteq \mathbb{R}_+$  as

$$(1) \quad \text{OHT}(\mathbf{x}, t) = C_p \int \theta(\mathbf{x}, t, z) \mathbf{v}(\mathbf{x}, t, z) \rho(\mathbf{x}, t, z) dz = C_p \int \frac{\theta(\mathbf{x}, t, p) \mathbf{v}(\mathbf{x}, t, p)}{g(\mathbf{x}, p)} dp,$$

where  $\rho$  is in-situ water density,  $C_p$  is the specific heat capacity of seawater, and  $g$  is gravitational acceleration. As shown here, the vertical integral can be computed in depth  $z$  or, using the hydrostatic relation, can be expressed as a function of pressure  $p$ . Given the range in density of seawater, pressure  $p$  (in units of decibars, dbar) and depth  $z$  (in units of meters, m) are approximately equal and are often used interchangeably in the oceanographic literature. Nonetheless, in-situ oceanographic observations, including those from the Argo profiling floats, predominately measure pressure and not depth, and thus here we mainly adopt the dependence on  $p$ .

As we can see from Equation (1), a direct calculation of OHT relies on the vertical structure of both temperature  $T$  (from which  $\theta$  is derived) and velocity  $\mathbf{v}$ . While temperature measurements have been collected throughout the global ocean from ships and moorings as well as autonomous platforms, the direct observation of subsurface ocean velocity is much more challenging. As a result, direct velocity measurements remain incredibly sparse in the global ocean below the surface ([Scott et al., 2010](#)). One common approach to address this issue exploits the fact that on large spatio-temporal scales, ocean flows are generally constrained to follow lines of constant pressure at any particular depth (i.e., the velocity is *geostrophic*). By combining this relationship with the assumption of hydrostatic balance, which is valid for large-scale geophysical flows, the vertical structure in the velocity field can be inferred from horizontal variations in the density field, given a known velocity field at just a single pressure level ([Talley et al., 2011](#); [Gray and Riser, 2014](#)). Because seawater density  $\rho$  depends only on  $T$ ,  $p$ , and salinity  $S$ , all relatively easy to measure beneath the ocean surface, this transformation provides a crucial way to estimate velocity, and correspondingly OHT, based on observations throughout the global ocean.

Mathematically, at any space-time point  $(\mathbf{x}, t)$ , the geostrophic velocity at pressure  $p$  can be expressed as the sum of  $\mathbf{v}_{\text{ref}}$ , the velocity at a fixed reference pressure  $p_0$ , and  $\mathbf{v}_{\text{rel}}$ , the difference between the geostrophic velocities at  $p$  and  $p_0$  as follows:

$$(2) \quad \mathbf{v}(p) = \mathbf{v}_{\text{ref}}(p_0) + \mathbf{v}_{\text{rel}}(p) = \mathbf{v}_{\text{ref}}(p_0) + \frac{1}{f} R \cdot \nabla_{\mathbf{x}} \Psi(p),$$

where  $R = [0, -1; 1, 0]$ ,  $f = 2\Omega \sin(y)$  is the Coriolis parameter which depends on the rotational rate of the Earth ( $\Omega = 7.2921 \times 10^{-5} \text{ rad s}^{-1}$ ) and latitude  $y$ , and the horizontal derivative operator  $\nabla_{\mathbf{x}}(\cdot) = \left[ \frac{\partial}{\partial x}, \frac{\partial}{\partial y} \right]^T$ . The dynamic height anomaly  $\Psi$  at any one space-time location is computed from the vertical integral of the inverse of density  $\rho$ ,

$$(3) \quad \Psi(p) := \Psi(S, T, p) = - \int_{p_0}^p \left( \frac{1}{\rho(S(p^*), T(p^*), p^*)} - \frac{1}{\rho(S_O, 0^\circ\text{C}, p^*)} \right) dp^*,$$

where  $S_O = 35.16504 \text{ g kg}^{-1}$ , and the limits of the integration are the reference pressure  $p_0$  and the level of interest  $p$ .

Bringing together Equations (1) – (3), concurrent measurements of  $T(p)$  and  $S(p)$ , together with an estimate of  $\mathbf{v}_{\text{ref}}$  at  $p_0$ , can be used to compute an observation-based estimate of OHT. While historically such observations have been sparse and unevenly sampled in space and time, over the past two decades the international oceanographic community has built a global array of autonomous instruments that provides exactly these measurements with unprecedented spatio-temporal coverage. The Argo array (Roemmich et al., 1998; Riser et al., 2016) consists of nearly 4000 autonomous profiling floats that collect subsurface measurements of  $T$ ,  $S$ , and  $p$  in the upper 2000 m of the ocean globally, with near-uniform sampling every  $3^\circ \times 3^\circ \times 10$  days in space and time. The number of floats has continuously increased since initial deployments began in the early 2000s, reaching the designed spatial coverage in 2007. The strength of Argo comes from its high sampling density and global, nearly uniform spatio-temporal coverage, along with its high-precision in-situ measurements (Riser et al., 2016). Each float follows a pre-determined cycle in which it starts by descending to a parking depth of 1000 dbar, then drifts for 9 days with the predominant currents at that depth, and subsequently sinks to a profiling depth of 2000 dbar before slowly ascending to the surface while measuring ocean variables with vertical resolution of up to 2 dbar for modern floats (Roemmich et al., 1998). The set of measurements during the ascent, along with the spatial location and time stamp for each cycle (determined from satellite positioning systems while at the surface), is called a *profile*. These data are transmitted to shore-based computing systems via satellite communications and made freely available to the public in near real time.

The dataset used in this study is based on Argo  $T(p)$  and  $S(p)$  profiles from throughout the global ocean, from January 2007 to December 2018, obtained from a January 2019 snapshot of the Argo Global Data Assembly Center (GDAC, Argo, 2020); see Figure 1a. Quality control criteria detailed in Section A of the Supplementary Material (Park et al., 2020) along with those of Kuusela and Stein (2018b) are applied to filter out problematic profiles. At each profile location,  $\Psi$  is computed from the measured  $T$  and  $S$  profiles according to Equation (3) with the TEOS-10 software library (McDougall and Barker, 2011), which is also used to calculate  $\theta$  from the measured variables. The reference pressure used to compute  $\Psi$  was set to 900 dbar to align with our choice of  $\mathbf{v}_{\text{ref}}$  (described below). The final dataset  $\mathcal{D}$  consists of 1,140,693  $\theta$ - $\Psi$  profiles that passed the quality control, with pressure levels ranging from 10 dbar to 900 dbar. This corresponds to 89.6% of all available profiles which passed the initial quality control of Kuusela and Stein (2018b). We avoided estimating any variables at pressure levels too close to the surface, i.e., less than 10 dbar, since only 67% of profiles could be retained in that case, due to a lack of very shallow observations in many profiles.

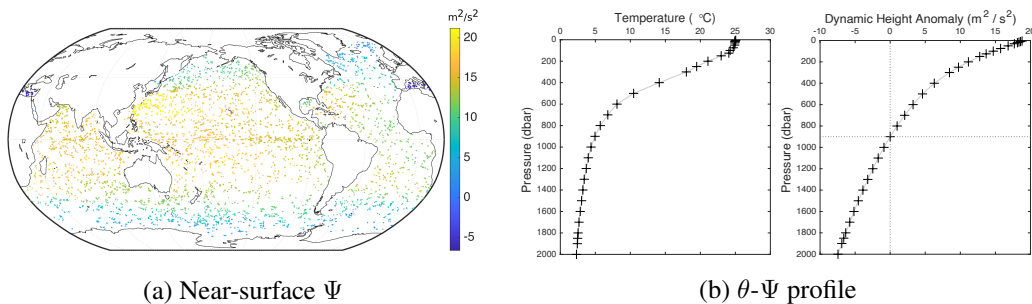


Fig 1: Visual illustration of the Argo dataset. (a) Locations of profiles collected in February 2017, colored by their dynamic height anomalies  $\Psi$  at 10 dbar referenced to  $p_0 = 900$  dbar. (b) A  $\theta$ - $\Psi$  profile for float ID 5900208 observed at  $19.4^\circ\text{S}$ ,  $154^\circ\text{E}$ , and 4 am UTC on Sep. 26, 2017. The dotted line on the  $\Psi$  profile indicates the reference pressure  $p_0 = 900$  dbar.

While the Argo dataset can be used to determine  $\mathbf{v}_{\text{rel}}$  according to Equation (2), a complete estimate of the absolute velocity  $\mathbf{v}$ , and consequently OHT, also requires an estimate of the reference velocity  $\mathbf{v}_{\text{ref}}$ . However, estimating  $\mathbf{v}_{\text{ref}}$  requires a separate treatment since  $\theta$ - $\Psi$  profiles does not contain direct information on  $\mathbf{v}_{\text{ref}}$ . In this study, we assume that the reference velocity is given as there are existing well-studied products for the absolute geostrophic velocity at the sea surface or at the Argo floats’ parking depth (see, e.g., [Lebedev et al., 2007](#); [Willis and Fu, 2008](#); [Ollitrault and Rannou, 2013](#); [Gray and Riser, 2014](#)). For the empirical analyses in Section 4, we adopt the reference geostrophic velocity estimates and mapping error estimates derived from Argo float trajectories at  $p_0 = 900$  dbar ([Gray and Riser, 2014](#)) at all profile spatio-temporal coordinates based on their nearest-neighbor grid point in the data product. These estimates are solely based on direct observations of the Argo float trajectories, which aligns well with our goal to quantify the geostrophic velocity and OHT based on autonomous in-situ observations. We note that the quality of the reference velocity estimate directly impacts the accuracy and uncertainty of the resulting estimate of absolute velocity and hence heat transport; improving the reference velocity field is, however, beyond the scope of the present work.

### 3. Statistical Methodology.

3.1. *Overview.* We first overview each component of the statistical methodology and explain how they bind together in a unified framework. The main procedural challenge can be understood as a combination of two classical statistical problems: spatio-temporal interpolation and latent variable modeling. Given  $\Psi$  profiles at some spatio-temporal coordinates, the velocity  $\mathbf{v}$  can be understood as a spatio-temporally dependent latent function in which the dependency structure is heterogeneous across the ocean and the time span. The OHT field, the final quantity of interest, presents similar spatio-temporal challenges as well. Neglecting these unique characteristics of the spatio-temporal (latent) variables could result in suboptimal OHT predictions.

To overcome these challenges, a two-stage procedure based on local Gaussian process regression (LGPR) is introduced. LGPR applied particularly to the Argo dataset ([Kuusela and Stein, 2018a](#)) has shown outstanding interpolation performance compared to that of previous state-of-the-art methods. We extend the work of [Kuusela and Stein \(2018a\)](#) by considering *latent LGPR*, which is specifically tailored to solving the statistical complications in estimating the OHT field. Based on the scientific framework in the previous section, the first stage of procedure estimates the dynamic height anomaly  $\Psi$  field at a series of fixed pressure levels, of which the spatial gradients provide the latent relative velocity  $\mathbf{v}_{\text{rel}}$  field according to Equation (2). Next, the results of this step are combined with an independent estimate of  $\mathbf{v}_{\text{ref}}$  to compute spot OHT values at the space-time locations of the Argo profiles using Equation (1). This integral can be calculated across any range of pressure levels, providing the capability to examine the contribution of different water layers to the total OHT. Conditional on the predicted spot OHT, these estimated OHT values are then interpolated to a regular spatio-temporal grid in the second stage of the LGPR procedure. We detail the LGPR framework in Section 3.2 and the latent LGPR with the two-stage procedure in Section 3.3.

We further improve the LGPR approach of [Kuusela and Stein \(2018a\)](#), which focuses on estimating a local space-time covariance model from detrended temperature observation whose mean field was estimated using OLS, by simultaneously estimating both the mean and the covariance parameters with an *approximate EM* algorithm. The procedure shares similarities with GLS. However, our EM procedure is able to account for the overlapping local moving windows of the LGPR covariance structure in a computationally efficient fashion when estimating the mean field. We detail the procedure in Section 3.4.

Predicting the gradient field from incomplete observations with a potentially under-specified mean field model may result in a concerning bias. By formalizing a procedure previously used by [Roemmich and Gilson \(2009\)](#), we provide in Section 3.5 an intuitive *de-biasing* procedure that effectively mitigates the bias in the predicted gradient and, if needed, the target field. The procedure captures the asymptotically valid bias field by correcting which improves the calibration of both gradient and target field.

**3.2. Spatio-temporal LGPR model.** We briefly review the LGPR model originally proposed for Argo mapping in [Kuusela and Stein \(2018a\)](#) motivated by [Haas \(1990, 1995\)](#), and illustrate the similarities and differences when adopting LGPR specifically for OHT interpolation. Consider a real-valued spatio-temporal random field of a quantity of interest  $\{\Upsilon(\mathbf{x}, t, p)\}_{\mathbf{x} \in \mathbb{X}, t \in \mathbb{T}}$  observed at a spatial location  $\mathbf{x} = (x, y)$  in the open ocean  $\mathbb{X} \subseteq \mathbb{R}^2$  with longitude  $x$  and latitude  $y$  in degrees; time  $t \in \mathbb{T} \subseteq [0, 365]$  in yeardays; and at some fixed pressure  $p$ . Hereafter, we will use  $\mathbf{s} = (\mathbf{x}, t)$  to denote a spatio-temporal coordinate. The response field  $\Upsilon$  can be either the dynamic height anomaly  $\Psi$  or the Ocean Heat Transport OHT, depending on the context, with the same model structure. We express the field as:

$$(4) \quad \Upsilon(\mathbf{x}, t, p) = m(\mathbf{x}, t, p) + a(\mathbf{x}, t, p) + \epsilon(\mathbf{x}, t, p),$$

where  $m(\mathbf{x}, t, p)$  denotes a large-scale climatological *mean field* with a seasonal cycle;  $a(\mathbf{x}, t, p)$  denotes an *anomaly field*, i.e., a transient deviation from the climatological mean, and  $\epsilon$  is a fine-scale *nugget* effect. The term *mean*, denoted by  $m$ , is adopted to specify  $\mathbb{E}[\Upsilon(\mathbf{x}, t, p)]$ , the deterministic mean of the process  $\Upsilon$ , whereas the term *anomaly*, and the notation  $a$ , refers to a residual process centered at zero. We drop  $p$  hereafter for brevity whenever the argument does not depend on the choice of  $p$ .

In this paper, we consider a *locally semiparametric* model in the sense that the mean field is assumed to be locally parametric whereas the anomaly field is locally nonparametric—specifically, a locally stationary Gaussian process. Nevertheless, both the mean and the anomaly field are actually nonparametric models since the semiparametric distinction happens only at local neighborhoods. Local polynomial regression ([Fan et al., 1997](#)), which we employ for the mean field, is already in itself a nonparametric method. The locally semiparametric model not only improves estimation efficiency by confining the parameter space but also matches our intent that the mean field explains the systematic large-scale patterns whereas the anomaly field captures the transient patterns.

The nugget effect  $\epsilon$  is assumed to locally be a Gaussian white noise process with mean zero and variance  $\sigma_\epsilon^2$  and independent of the anomaly field  $a$ . This distributional assumption leads to a closed-form predictive distribution, enabling convenient uncertainty quantification. Even though the Gaussian nugget is widely adopted in the literature, [Kuusela and Stein \(2018a\)](#) pointed out that the Gaussian nugget may be insufficient to account for the heavy-tailed nugget distribution of subsurface temperature data in certain parts of the ocean. An extension to a heavy-tailed Student nugget ([Kuusela and Stein, 2018a](#)) is possible. However, we only focus on the Gaussian nugget in this paper for simplicity.

We let the pilot model of the large-scale mean field  $m(\mathbf{x}, t)$  to be a *local polynomial regression* ([Fan et al., 1997](#)) with uniform weights ([Stone, 1980](#)). In particular, within a small circular spatial window  $\mathcal{W}_{\lambda_G}(\mathbf{x}^*) = \{\mathbf{x} : \|\mathbf{x} - \mathbf{x}^*\|_G \leq \lambda_G\}$ , where  $\|\cdot\|_G$  denotes the distance in WGS84 coordinates and  $\lambda_G$  is a positive bandwidth that controls the size of the spatial neighborhoods in estimating the coefficients, we let

$$(5) \quad m(\mathbf{x}, t) = \beta_0 + \beta_x x_c + \beta_y y_c + \beta_{xy} x_c y_c + \beta_{x^2} x_c^2 + \beta_{y^2} y_c^2 + \sum_{k=1}^K \left[ \beta_{c_k} \cos\left(\frac{2\pi kt}{365}\right) + \beta_{s_k} \sin\left(\frac{2\pi kt}{365}\right) \right],$$

where  $x_c := x - x^*$  and  $y_c := y - y^*$  are spatial coordinates centered around  $x^*$  and  $y^*$ , and  $K$  is a predefined maximum number of harmonics. The first line in Equation (5) captures the local spatial structure of the mean field, while the second line models the seasonal cycle within the window. This regression model with  $K = 6$  has been successfully adopted in the oceanographic literature to model the mean field of Argo observations (Ridgway, Dunn and Wilkin, 2002; Roemmich and Gilson, 2009), albeit with slight different estimation method.

The anomaly field is modeled using a zero-mean locally stationary Gaussian process which is i.i.d. over the years and whose distance metric is defined as the Mahalanobis distance both in terms of space and time (Kuusela and Stein, 2018a). Let  $\mathbf{s}^* = (x^*, t^*)$  be a space-time (intra-annual) grid point for which a prediction is desired. Within a small spatio-temporal window  $\widetilde{\mathcal{W}}_\lambda(\mathbf{s}^*) = \mathcal{W}_{\lambda_G}(\mathbf{x}^*) \times [t^* - \lambda_t, t^* + \lambda_t]$  around  $\mathbf{s}^*$ , we let

$$(6) \quad a_i \stackrel{\text{i.i.d.}}{\sim} \text{GP}(0, k(\mathbf{s}_1, \mathbf{s}_2; \boldsymbol{\xi})), \quad i = 1, \dots, I,$$

where the index  $i$  refers to years,  $k(\mathbf{s}_1, \mathbf{s}_2; \boldsymbol{\xi}) = k(x_1 - x_2, y_1 - y_2, t_1 - t_2; \boldsymbol{\xi})$  is a stationary space-time covariance function depending on non-negative hyperparameters  $\boldsymbol{\xi} = (\phi, \xi_x, \xi_y, \xi_t)^\top$  detailed below and  $\boldsymbol{\lambda} = (\lambda_G, \lambda_t)$  are positive bandwidth parameters with an additional parameter  $\lambda_t$  to control the size of the temporal neighborhood.

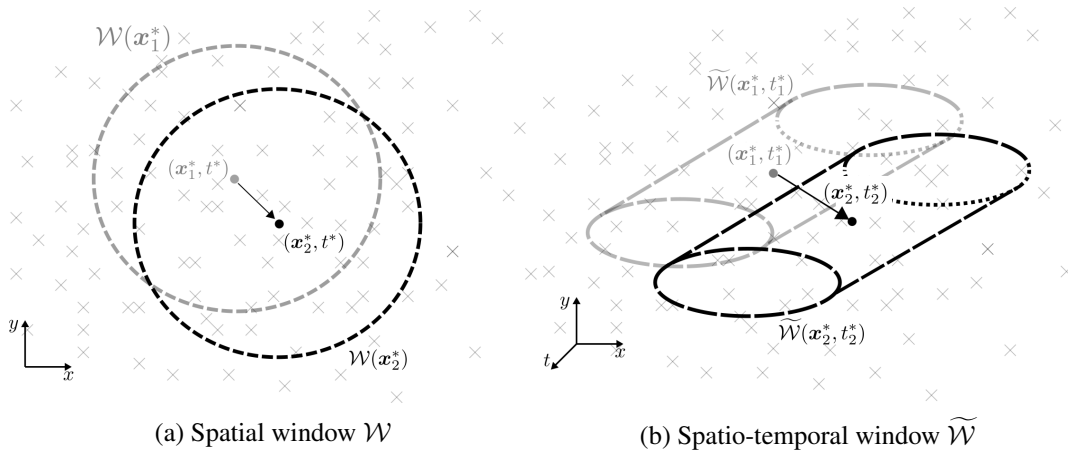


Fig 2: Local windows adopted in the spatio-temporal LGPR model.

Figure 2 illustrates the circular local windows  $\mathcal{W}$  and cylindrical windows  $\widetilde{\mathcal{W}}$  adopted for the mean field and the anomaly field, respectively. In  $\mathbb{R}^2 \times [0, 365]$  the spatio-temporal window  $\widetilde{\mathcal{W}}_\lambda(\mathbf{s}^*)$  is a subset of  $\mathcal{W}_\lambda(\mathbf{x}^*)$  for any spatial location  $\mathbf{x}^*$  so the anomaly field flexibly captures the local interannual temporal signal on top of the parametric climatological seasonal cycle in Equation (5). This nested construction is the reason we use the iterative EM instead of GLS for jointly estimating the relevant parameters, as we will see in Section 3.4. We also note that the circular window used here is more natural than the square window used in Kuusela and Stein (2018a).

Bandwidth choice entails a trade-off in both computational and statistical aspects. The larger the size of the window, the larger the computational cost. Given that the computational complexity grows in a cubic order to the number of observations within  $\widetilde{\mathcal{W}}$ , the bandwidths affect  $O(\lambda_G^6 \lambda_t^3)$  computational cost. While access to high performance computing makes estimation and prediction feasible for larger bandwidth parameters, larger window sizes do not equate to better prediction due to a bias-variance trade-off. Considering that ocean dynamics

are globally non-stationary, excessively large windows are more likely to violate the assumption that the Gaussian process is stationary within the window, resulting in a concerning bias. On the contrary, too small window size suffers from a higher estimation variance or even fail to make a prediction, e.g., near the coastal boundary, due to scarce data within the window. Therefore, it is recommended to choose window sizes with which the computation and the locally stationary assumption are both feasible without losing essential boundary dynamics.

Care has to be taken in specifying the local windows  $\mathcal{W}_\lambda$  and  $\widetilde{\mathcal{W}}_\lambda$  for the OHT field ( $\Upsilon = \text{OHT}$ ) near the equator since geostrophic balance, and thus Equation (2), does not hold as the Coriolis parameter  $f$  approaches zero. We threshold the windows to ameliorate this issue by masking out the tropical latitude band  $[-\zeta, \zeta]$  for some positive parameter  $\zeta$ . More refined methods might be possible, such as using a  $\beta$ -plane approximation (Lagerloef et al., 1999); these are, however, beyond the scope of the present study.

Unlike Kuusela and Stein (2018a), in which an exponential covariance function was used, we choose the Matérn covariance function (Stein, 1999) to ensure that the process is differentiable which is required for estimating the velocities. Since a Gaussian process with Matérn covariance with smoothness parameter  $\nu$  is  $\lceil \nu \rceil - 1$  times differentiable, we set  $\nu$  to be  $3/2$  to ensure first-order differentiability. Specifically,

$$(7) \quad k(\mathbf{s}_1, \mathbf{s}_2; \boldsymbol{\xi}) = \phi \left( 1 + \sqrt{3} \|\Delta \mathbf{s}\|_{\mathbf{A}^{-1}} \right) \exp \left( -\sqrt{3} \|\Delta \mathbf{s}\|_{\mathbf{A}^{-1}} \right),$$

where  $\phi$  is the GP variance,  $\|\Delta \mathbf{s}\|_{\mathbf{A}^{-1}} = \sqrt{\Delta \mathbf{s}^\top \mathbf{A}^{-1} \Delta \mathbf{s}}$  is the Mahalanobis norm with  $\Delta \mathbf{s} = \mathbf{s}_1 - \mathbf{s}_2$  and  $\mathbf{A} = \mathbf{A}(\boldsymbol{\xi})$  is a positive definite matrix parameterized by  $\boldsymbol{\xi}$ . Non-diagonal elements of  $\mathbf{A}$  represent rotation of the spatio-temporal space although at the expense of three additional parameters. Given that we estimate the Gaussian process locally, the number of parameters increases in the order of the number of local windows. A diagonal covariance parameter matrix  $\mathbf{A} = \text{diag}(\xi_x^2, \xi_y^2, \xi_t^2)$  is therefore chosen to efficaciously restrict the parameter space since we did not see empirical improvements in our application from adding extra off-diagonal parameters, agreeing with Kuusela and Stein (2018a).

A convenient feature of a Gaussian process is that the first-order derivative is still a Gaussian process (Banerjee, Gelfand and Sirmans, 2003; Rasmussen and Williams, 2006). That is, the joint process  $[a_i, \nabla_{\mathbf{x}} a_i]$  is a multivariate Gaussian process: For any  $\mathbf{s}_1, \mathbf{s}_2 \in \widetilde{\mathcal{W}}_\lambda(\mathbf{s}^*)$ ,

$$(8) \quad \begin{bmatrix} a_i \\ \nabla_{\mathbf{x}} a_i \end{bmatrix} \stackrel{\text{i.i.d.}}{\sim} \text{GP} \left( \mathbf{0}, \begin{bmatrix} k(\mathbf{s}_1, \mathbf{s}_2) & \nabla_{\mathbf{x}_2} k(\mathbf{s}_1, \mathbf{s}_2)^\top \\ \nabla_{\mathbf{x}_1} k(\mathbf{s}_1, \mathbf{s}_2) & \nabla_{\mathbf{x}_1} \nabla_{\mathbf{x}_2} k(\mathbf{s}_1, \mathbf{s}_2) \end{bmatrix} \right),$$

where the analytic forms for the gradient and the Hessian of the covariance function are provided in Section B of Supplementary Material (Park et al., 2020). This feature leads to an important consequence: by Equation (2), the geostrophic velocity field  $\mathbf{v}$  retains the same LGPR structure (4), where the mean field is given by the local spatial coefficients  $\beta_x$  and  $\beta_y$  of the local polynomial model (5), and the anomaly field is a locally stationary Gaussian process given in (8). Thus, the predictive distribution of  $\mathbf{v}(\mathbf{s}^*)$ , where the year of  $t^*$  is  $i$ , is

$$\mathbf{v}(\mathbf{s}^*) | \mathcal{D} \sim \text{N} \left( \mu_{\mathbf{v}_{\text{ref}}}(\mathbf{s}^*) + f^{-1} R \left[ \nabla_{\mathbf{x}} m_\Psi(\mathbf{s}^*; \boldsymbol{\beta}_\Psi) + \nabla_{\mathbf{x}} k_{\Psi, i}^\top(\mathbf{s}^*) \mathbf{K}_{\Psi, i}^{-1} (\Psi(\mathbf{s}_i) - m_\Psi(\mathbf{s}_i)) \right], \right. \\ \left. \sigma_{\mathbf{v}_{\text{ref}}}^2(\mathbf{s}^*) + f^{-2} R \left[ \nabla_{\mathbf{x}} \nabla_{\mathbf{x}} k(\mathbf{s}^*, \mathbf{s}^*) - \nabla_{\mathbf{x}} k_{\Psi, i}^\top(\mathbf{s}^*) \mathbf{K}_{\Psi, i}^{-1} \nabla_{\mathbf{x}} k_{\Psi, i}(\mathbf{s}^*) \right] R^\top \right),$$

where  $\mu_{\mathbf{v}_{\text{ref}}}$  and  $\sigma_{\mathbf{v}_{\text{ref}}}^2$  are the reference velocity estimate and its mapping uncertainty,  $\mathbf{s}_i$  are the spatio-temporal coordinates of  $\mathbf{s}_{\mathcal{D}}$  within  $\widetilde{\mathcal{W}}(\mathbf{s}^*)$  for the  $i$ -th year,  $\mathbf{s}_{\mathcal{D}}$  is a collection of all observed spatio-temporal coordinates in  $\mathcal{D}$ ,  $k_{\Psi, i}(\mathbf{s}^*) = [k(\mathbf{s}, \mathbf{s}^*; \boldsymbol{\xi}_\Psi)]_{\mathbf{s} \in \mathbf{s}_i}$ ,  $\mathbf{K}_{\Psi, i} = [k(\mathbf{s}_j, \mathbf{s}_k; \boldsymbol{\xi}_\Psi)]_{\mathbf{s}_j, \mathbf{s}_k \in \mathbf{s}_i} + \sigma_{\Psi, \epsilon}^2 \mathbf{I}_{\mathbf{s}_i}$  is the associated  $|\mathbf{s}_i| \times |\mathbf{s}_i|$  Gram matrix of  $k$  plus the nugget variance. This notation will be repeatedly used hereafter for both  $\Psi$  and OHT depending on the context.

3.3. *Latent LGPR and two-stage estimation procedure.* Our overarching inferential goal is to compute the predictive mean  $\mathbb{E}[\text{OHT} \mid \mathcal{D}]$  for point prediction, and ultimately the predictive distribution of  $\text{OHT} \mid \mathcal{D}$ . The main complication in estimating the OHT field using definition (1) is that  $\mathbf{v}$  is a latent spatio-temporal field whose realizations are not observable by the floats. Only potential temperature  $\theta$  and dynamic height anomaly  $\Psi$  profiles are observed, as in Section 2. In this section, we link the final field of interest OHT with the  $\Psi$  field via two-stage estimation approach.

Within a small spatio-temporal window  $\widetilde{\mathcal{W}}_\lambda(\mathbf{s}^*)$  around  $\mathbf{s}^*$ , OHT can be expressed as a *latent LGPR* model as follows.

$$(9) \quad \begin{aligned} \Psi_i(p) &\stackrel{\text{i.i.d.}}{\sim} \text{GP}(m_\Psi, k(\mathbf{s}_1, \mathbf{s}_2; \xi_\Psi)), \quad p = p_1, \dots, p_P, \\ \text{OHT}_i \mid \mathbf{v}_1, \dots, \mathbf{v}_I &\stackrel{\text{i.i.d.}}{\sim} \text{GP}(m_{\text{OHT}}, k(\mathbf{s}_1, \mathbf{s}_2; \xi_{\text{OHT}})) \end{aligned}$$

where  $m_\Upsilon$  is a mean field (5) of  $\Upsilon = \Psi$  or  $\Upsilon = \text{OHT}$  within the spatial window  $\mathcal{W}_{\lambda_G}(\mathbf{x}^*)$ , and  $\mathbf{v}_i$  is a  $\mathbf{s}_i \times P$ -dimensional matrix with respect to  $P$  pressure levels.

Figure 3 illustrates the latent structure of (9). Notice that the OHT variable,  $\text{OHT} \propto \int \theta(p) \cdot \mathbf{v}(p) dp$ , is only half colored since the temperature  $\theta$  is observed, whereas the velocity  $\mathbf{v}$  is not. The spatio-temporal dependence of both  $\Psi$  and OHT is encoded with edges stemming from  $\mathbf{s}$ . By Equation (8),  $\mathbf{v}$  retains the spatio-temporal LGPR structure, and we can leverage the prediction of  $\mathbf{v}$  under the LGPR model to obtain an estimate of the unobserved velocity. This model effectively incorporates the key spatio-temporal properties, i.e., the complex spatio-temporal dependence structure and the global non-stationarity, of both the latent field  $\mathbf{v}$  and the final quantity of interest OHT in a data-driven manner.

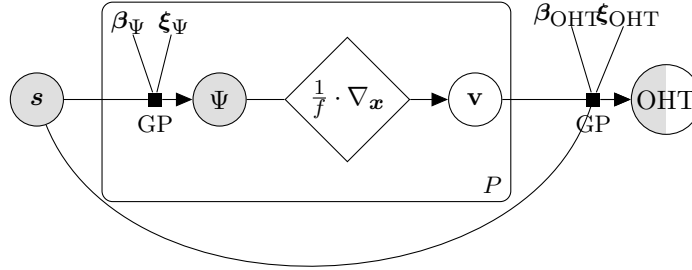


Fig 3: Graphical representation of latent LGPR for OHT quantification. A grey node indicates an observed variable, while a white node indicates a latent variable. Each variable represents a  $|\mathbf{s}_D|$ -dimensional vector. A diamond-shaped node denotes a deterministic operation.

Consider the simplest case where  $P = 1$ , i.e., the heat transport at a fixed pressure  $p^*$  which is  $\text{OHT}(\mathbf{s}) = C_p/g(\mathbf{x}, p^*) \cdot \theta(\mathbf{s}, p^*) \cdot \mathbf{v}(\mathbf{s}, p^*)$ . Since  $\text{OHT}(\mathbf{s}) \mid \mathcal{D} \propto (\text{OHT}(\mathbf{s}) \mid \mathbf{v}(\mathbf{s}_i), \mathcal{D}) \cdot (\mathbf{v}(\mathbf{s}_i) \mid \mathcal{D})$  and the model (9) implies that the predictive distributions of both  $\text{OHT}(\mathbf{s}) \mid \mathbf{v}(\mathbf{s}_i)$  and  $\mathbf{v}(\mathbf{s}_i)$  are Gaussian, the predictive distribution of OHT is therefore also Gaussian with a closed-form mean and variance. Details are provided in Section E of the Supplementary Material (Park et al., 2020).

For multiple pressure levels, the predictive mean  $\mathbb{E}[\text{OHT} \mid \mathcal{D}]$ , used as a point predictor, can be similarly derived using the law of iterated expectations. For any  $\mathbf{s}^*$  within  $\widetilde{\mathcal{W}}(\mathbf{s}^*)$ ,

$$(10) \quad \begin{aligned} \mathbb{E}[\text{OHT}_i(\mathbf{s}^*) \mid \mathcal{D}] &= \mathbb{E}[\mathbb{E}[\text{OHT}_i(\mathbf{s}^*) \mid \widehat{\mathbf{v}}(\mathbf{s}_i, p_1), \dots, \widehat{\mathbf{v}}(\mathbf{s}_i, p_P), \mathcal{D}] \mid \mathcal{D}], \\ &= m_{\text{OHT}}(\mathbf{s}^*) + k_{\text{OHT}}(\mathbf{s}^*, \mathbf{s}_i) \mathbf{K}_{\text{OHT}, i}^{-1} \left[ \widetilde{\text{OHT}}(\mathbf{s}_i) - m_{\text{OHT}}(\mathbf{s}_i) \right], \end{aligned}$$

$$(11) \quad \widetilde{\text{OHT}}(\mathbf{s}) = C_p \int_{p_1}^{p_P} \frac{\theta(\mathbf{s}, p) \cdot \mathbb{E}[\mathbf{v}(\mathbf{s}, p) | \mathcal{D}]}{g(\mathbf{x}, p)} dp, \quad \forall \mathbf{s} \in \mathcal{S}_{\mathcal{D}}.$$

Procedurally, this can be viewed as a *two-stage* method where we first construct the predicted OHT data set  $\widetilde{\mathcal{D}} = \{(\mathbf{s}, \widetilde{\text{OHT}}(\mathbf{s})) : \mathbf{s} \in \mathcal{S}_{\mathcal{D}}\}$  in the first stage. We then compute the conditional mean  $\mathbb{E}(\text{OHT} | \widetilde{\mathcal{D}})$  using the generated dataset in the second stage; see Algorithm 1. In practice,  $\Psi$  can only be evaluated at a finite set of  $P$  pressure levels, which leads us to approximate the vertical integral when computing  $\widetilde{\text{OHT}}$ . We employ piecewise cubic Hermite interpolation (PCHIP, Fritsch and Carlson (1980)) followed by numerical integration. PCHIP is well-suited for this task since it constructs a piecewise cubic interpolant that respects the monotonicity of the data, thereby avoiding spurious bumps typical of alternative interpolation methods (Barker and McDougall, 2020).

The predictive variance of OHT can be expressed using the law of total variance. For any  $\mathbf{s}^*$  within  $\widetilde{\mathcal{W}}(\mathbf{s}^*)$ ,

$$(12) \quad \begin{aligned} \mathbb{V}[\text{OHT}_i(\mathbf{s}^*) | \mathcal{D}] &= \left[ \phi_{\text{OHT}} + \sigma_{\epsilon, \text{OHT}}^2 - k_{\text{OHT}}(\mathbf{s}^*, \mathbf{s}_{i \cdot}) \mathbf{K}_{\text{OHT}, i}^{-1} k_{\text{OHT}}(\mathbf{s}_{i \cdot}, \mathbf{s}^*) \right] \\ &\quad + k_{\text{OHT}}(\mathbf{s}^*, \mathbf{s}_{i \cdot}) \mathbf{K}_{\text{OHT}, i}^{-1} \mathbb{V}[\text{OHT}(\mathbf{s}_{i \cdot}) | \mathcal{D}] \mathbf{K}_{\text{OHT}, i}^{-1} k_{\text{OHT}}(\mathbf{s}_{i \cdot}, \mathbf{s}^*). \end{aligned}$$

This decomposition shows that the predictive variance of OHT is a combination of (i) variation solely from the second stage (the first line), and (ii) the uncertainty that propagates from the first stage to the second stage (the second line). Even though the point predictor  $\mathbb{E}[\text{OHT} | \mathcal{D}]$  can be obtained without approximations using Equation (10), the predictive variance would require the knowledge of the vertical correlation to compute  $\mathbb{V}[\text{OHT}(\mathbf{s}_{i \cdot}) | \mathcal{D}]$ . This ultimately necessitates an approximation or a conservative upper bound to the predictive variance. Incorporating the vertical correlation in addition to spatio-temporal correlation is still an active area of research (see e.g. Yarger, Stoev and Hsing, 2020).

**3.4. Approximate Expectation-Maximization algorithm.** Given the Argo data<sup>1</sup>  $\mathcal{D} := \{(\Upsilon_{ij}, \mathbf{s}_{ij}) : i = 1, \dots, I; j = 1, \dots, n_i\}$  (either  $\Psi$  or  $\text{OHT} | \Psi$ ), we seek to estimate a collection of  $\beta$  denoted by  $\mathbf{B} = \{\beta(\mathbf{x}^*) : \mathbf{x}^* \in \mathcal{X}\}$  and a collection of  $\xi$  denoted by  $\Xi = \{\xi(\mathbf{s}^*) : \mathbf{s}^* \in \mathcal{S}\}$ , where  $\mathcal{S} = \mathcal{X} \times \mathcal{T}$  is a set of target spatio-temporal coordinates  $\mathbf{s}^* = (\mathbf{x}^*, t^*)$ , since the LGPR model specifies the covariance structure on the spatio-temporal window  $\widetilde{\mathcal{W}}(\mathbf{s}^*)$  nested within the spatial window  $\mathcal{W}(\mathbf{x}^*)$  on which the mean field structure is defined. We wish to find the parameters that maximize the likelihood function  $\mathcal{L}(\mathbf{B}, \Xi)$ ; however, a closed-form solution is not available for our LGPR model. We therefore employ an approximate EM algorithm (Dempster, Laird and Rubin, 1977), resulting in a *block coordinate ascent* algorithm, to jointly estimate all of the parameters.

We update the parameters at iteration  $l = 0, 1, \dots$  as follows:

$$\begin{aligned} \text{(E-Step)} \quad & \mathbf{B}^{(l+1)} = \operatorname{argmax}_{\mathbf{B}} \widetilde{\mathcal{L}}(\mathbf{B} | \Xi^{(l)}) \\ \text{(M-Step)} \quad & \Xi^{(l+1)} = \operatorname{argmax}_{\Xi} \mathcal{L}(\Xi | \mathbf{B}^{(l+1)}), \end{aligned}$$

where the initial guess  $\Xi^{(0)}$  corresponds to a set of identity covariance matrices, and therefore assuming that the process is spatio-temporally uncorrelated within each spatial window  $\mathcal{W}$ .  $\widetilde{\mathcal{L}}$  is an approximated  $\mathcal{L}$  which we will detail subsequently. At first glance, the above steps look like an alternating maximization (AM) algorithm (Csiszar and Tusnady, 1984), which indeed can be viewed as a special case of the EM algorithm as first suggested by Neal and

<sup>1</sup>Even though  $\mathcal{D}$  is originally defined as a collection of the triplets  $(\theta, \Psi, \mathbf{s})$  as in Algorithm 1, we redefine  $\mathcal{D}$  as duplets with a slight abuse of notation for this section to better focus on the procedure.

Hinton (1998). See Section C of the Supplementary Material (Park et al., 2020) for how they are connected under our setup. This EM algorithm is a generalization of Kuusela and Stein (2018a) since the MLE of the covariance parameters in Kuusela and Stein (2018a) corresponds to the EM algorithm with  $l = 0$ , which ignores the spatio-temporal correlation when estimating the mean field. Empirical improvement over Kuusela and Stein (2018a) in predictive performance is demonstrated in Section G.2 of the Supplementary Material.

The **M-Step** is essentially obtaining the maximum likelihood estimator (MLE) of  $\Xi$  from the residuals  $\tilde{\Upsilon}_{ij}^{(l+1)} := \Upsilon_{ij} - \hat{m}^{(l+1)}(s_{ij}), \forall i, j$ , where the estimated mean field  $\hat{m}^{(l+1)}$  is constructed based on the parameters  $\beta^{(l+1)}(\mathbf{x}^*)$  updated in the previous **E-Step**. For every  $\mathbf{s}^* \in \mathcal{S}$ ,

$$\mathcal{L}(\xi(\mathbf{s}^*) | \beta^{(l+1)}(\mathbf{x}^*)) = \prod_{i=1}^I p(\tilde{\Upsilon}_i^{(l+1)}; \xi(\mathbf{s}^*)),$$

where  $\tilde{\Upsilon}_i^{(l+1)}$  is a vector of  $\tilde{\Upsilon}_{ij}^{(l+1)}$ 's within the window  $\tilde{\mathcal{W}}(\mathbf{s}^*)$  in a specific year  $i$ , and  $p(\tilde{\Upsilon}_i^{(l+1)}; \xi(\mathbf{s}^*))$  is the pdf of the multivariate Gaussian distribution with zero mean and covariance matrix  $\mathbf{K}_i(\xi(\mathbf{s}^*)) + \sigma_\epsilon^2(\mathbf{s}^*)\mathbf{I}_{n_i}$ . To solve the **M-Step**, we adopted the BFGS quasi-Newton algorithm (Nocedal, 1980) in the empirical studies in Sections 4 and 5.

**E-Step** updates the deterministic mean field accounting for the spatio-temporal correlation of the residuals  $\tilde{\Upsilon}^{(l)}$  learned in the previous **M-Step**. This step is analogous to the GLS estimator in regression kriging literature to resolve the sub-optimality of OLS (Cressie, 1993) and shares a similarity with iterative GLS (Gray and Riser, 2015) adopted previously for Argo data. However, in our LGPR model, using the GLS estimator is not straightforward due to the nested temporal window  $\tilde{\mathcal{W}}$  within the spatial window  $\mathcal{W}$ , which limits the availability of the correlations at large temporal lags. To aggregate the local spatio-temporal covariance structures of  $\tilde{\mathcal{W}}$  into the spatial window  $\mathcal{W}$ , we employ the Vecchia approximation (Vecchia, 1988) which confines the aggregated covariance structure by thresholding the temporal lag outside of each  $\tilde{\mathcal{W}}$  in the conditional distribution. We note that this approach is different from block covariance tapering, and the Vecchia approximation is known to have advantages over covariance tapering (Stein, 2013).

The Vecchia approximation (Vecchia, 1988) is a natural choice both from the perspective of LGPR modeling and computational efficiency. Choosing uniform weights on each spatio-temporal window  $\tilde{\mathcal{W}}$ , we hard-threshold the conditional spatio-temporal dependency along the temporal axis in the anomaly field within  $2\lambda_t$  temporal lag of the target time point  $t^*$ . This implies that the LGPR model assumes observations within  $\tilde{\mathcal{W}}$  to be uncorrelated beyond the temporal window. Such a structure is reflected in the approximate likelihood function via Vecchia approximation. Additionally, this choice yields a closed-form **E-Step** resembling a GLS-like estimator, for which the details are given in Section D of Supplementary Material.

The overall EM procedure (**E-Step** and **M-Step**) leads to a computationally efficient algorithm since these steps can be viewed as a *gather-and-broadcast* algorithm. The **M-Step** can be performed fully in parallel across each  $\tilde{\mathcal{W}}$  once the residuals have been broadcast to each computing node. The **E-Step** then gathers the estimated covariance structures from each computing node and updates the aggregated mean parameter within  $\mathcal{W}$ . This parallelization leads to major computational benefits since the main computational bottlenecks of the procedure are the numerical optimizations required in the **M-Step** as opposed to the **E-Step** where the closed form solution is fast to compute.

**3.5. Debiasing the mean field.** In this section, we describe a simple debiasing procedure to account for potential mean field model misspecification. We have noticed that climate scientists oftentimes compute the empirical mean of the estimated anomaly fields across years

and add that back to the mean field to make the resulting estimate of the anomaly fields temporally centered at zero (e.g., [Roemmich and Gilson, 2009](#)). We formalize this procedure and demonstrate that it is a legitimate approach to (partially) identifying model misspecifications and correcting them. For the LGPR model (4), model misspecification may arise in both the mean and the covariance structure. Specifically, we focus on a potentially misspecified mean field, since inferring the climatological mean is of key interest in this application, and a bias arising from mean field misspecification propagates to the localized anomaly fields which leads to biased inference and prediction of the anomalies. The LGPR model (4) utilizes a mean field model  $m$  given in Equation (5) which is inspired by previous work in the oceanographic literature ([Ridgway, Dunn and Wilkin, 2002](#); [Roemmich and Gilson, 2009](#)). Even though this model is known to work well for simple oceanographic variables, such as temperature and salinity, the model may have trouble representing the mean of the OHT or  $\Psi$  fields with sharp fronts and other localized patterns, which further motivates us to use a bias-correction procedure in this application.

The predictive mean  $\hat{\Upsilon}(\mathbf{s}^{**}) := \mathbb{E}(\Upsilon(\mathbf{s}^{**}) \mid \mathcal{D})$ , for any  $\mathbf{s}^{**} \in \widetilde{\mathcal{W}}(\mathbf{s}^*)$ , is an unbiased estimator of the true mean field  $\mathbb{E}(\Upsilon(\mathbf{s}^{**})) = m(\mathbf{s}^{**})$  if the assumed mean field model for  $\Upsilon$  is well-specified following the construction (4). That is, when the year of  $\mathbf{s}^{**}$  is  $i$ ,

$$(13) \quad \mathbb{E} \left[ \hat{\Upsilon}_i(\mathbf{s}^{**}) \right] = \mathbb{E} \left[ m(\mathbf{s}^{**}) + k_i^\top(\mathbf{s}^{**}) \mathbf{K}_i^{-1} (\Upsilon_i(\mathbf{s}_i) - m(\mathbf{s}_i)) \right] \stackrel{(*)}{=} m(\mathbf{s}^{**}).$$

Suppose the analyst was oblivious to the true mean field  $m$  and misspecified the mean field model as  $\mathbb{E}_A(\Upsilon(\mathbf{s}^{**})) := m(\mathbf{s}^{**}) + B(\mathbf{s}^{**})$  by introducing a non-zero bias field  $B$ . Here  $\mathbb{E}_A$  denotes the assumed expectation under the analyst's model. The predictive mean  $\hat{\Upsilon}(\mathbf{s}^{**})$  under the misspecified model becomes

$$\hat{\Upsilon}_i(\mathbf{s}^{**}) = \mathbb{E}_A(\Upsilon(\mathbf{s}^{**})) + k_i^\top(\mathbf{s}^{**}) \mathbf{K}_i^{-1} (\Upsilon_i(\mathbf{s}_i) - \mathbb{E}_A(\Upsilon_i(\mathbf{s}_i))).$$

Then,  $(*)$  in Equation (13) no longer holds but instead

$$(14) \quad \mathbb{E} \left[ \hat{\Upsilon}_i(\mathbf{s}^{**}) \right] - m(\mathbf{s}^{**}) = B(\mathbf{s}^{**}) - k_i^\top(\mathbf{s}^{**}) \mathbf{K}_i^{-1} B(\mathbf{s}_i).$$

As the observations  $\mathbf{s}_i$  get denser within  $\widetilde{\mathcal{W}}(\mathbf{s}^*)$ , Equation (14) essentially converges to zero, and thus  $\hat{\Upsilon}_i \rightarrow \Upsilon_i$  for every year  $i$  under infill asymptotics, despite the misspecification of the mean field  $m$ . See [Stein \(1999, Chapter 4, Theorem 8\)](#) for a rigorous statement.

Given  $I$  years of observations, we estimate  $B(\mathbf{s}^{**})$  using the negative average anomaly

$$(15) \quad \begin{aligned} \hat{B}(\mathbf{s}^{**}) &= -\frac{1}{I} \sum_{i=1}^I k_i^\top(\mathbf{s}^{**}) \mathbf{K}_i^{-1} (\Upsilon_i(\mathbf{s}_i) - \mathbb{E}_A(\Upsilon(\mathbf{s}^{**}))) \\ &= \mathbb{E}_A(\Upsilon(\mathbf{s}^{**})) - \frac{1}{I} \sum_{i=1}^I \hat{\Upsilon}_i(\mathbf{s}^{**}) \xrightarrow{I \rightarrow \infty, \text{infill}} \mathbb{E}_A(\Upsilon(\mathbf{s}^{**})) - \mathbb{E}(\Upsilon(\mathbf{s}^{**})) = B(\mathbf{s}^{**}). \end{aligned}$$

This leads to a bias-corrected mean field  $\mathbb{E}_A^{\text{new}}(\Upsilon) = m + B - \hat{B}$ , which asymptotically converges to the true mean field  $m$  assuming that the  $\Upsilon$  fields are observed densely enough for every year and that we have observations from a large enough number of years.

The mean field misspecification affects the estimation of both the mean and the anomaly fields since we assumed the true mean field is  $m + B$  when initially computing  $\hat{m}$ , and consequently assumed  $\mathbb{E}_A(a_i(\mathbf{s}_i)) = 0$ , when in reality  $\mathbb{E}(a_i(\mathbf{s}_i)) = -B(\mathbf{s}_i)$ , when estimating the covariance parameters  $\Xi$  before correcting the bias. After the bias is identified, we re-estimate the covariance parameters  $\Xi$  based on the corrected residuals  $\Upsilon_i(\mathbf{s}_i) - \hat{m}(\mathbf{s}_i) + \hat{B}(\mathbf{s}_i)$ , for all  $i = 1, \dots, I$ , utilizing the **M-Step** of the EM procedure. The re-estimation step ensures that

the covariances are computed from the correct model structure (4) under which the anomaly field is truly centered at zero asymptotically. We then recompute the interpolated fields  $\hat{\Upsilon}$  based on the updated covariance parameters.

The proposed debiasing method is directly applicable not only to  $\Psi$  or OHT| $\Psi$  in the latent LGPR model (9) but also to the latent velocity field  $\mathbf{v}$  without additional computational burden. Recall that applying the deterministic operation  $\frac{1}{f} \cdot \nabla_{\mathbf{x}}$  on the  $\Psi$  field yields the  $\mathbf{v}$  field. Since the operation only consists of linear operators, our bias estimate for the  $\mathbf{v}$  field is

$$(16) \quad \frac{1}{f} \cdot \widehat{\nabla_{\mathbf{x}^{**}} B(\mathbf{s}^{**})} = -\frac{1}{f} \cdot \frac{1}{I} \sum_{i=1}^I \nabla_{\mathbf{x}^{**}} k_i^\top(\mathbf{s}^{**}; \hat{\boldsymbol{\xi}}_\Psi) \mathbf{K}_i^{-1}(\hat{\boldsymbol{\xi}}_\Psi) (\Psi(\mathbf{s}_i) - \hat{m}_\Psi(\mathbf{s}_i)).$$

As the analytic form of the gradient of the Matérn covariance function is available (see Section B of the Supplementary Material (Park et al., 2020)), the additional computational burden to calculate the bias of  $\mathbf{v}$  is marginal in the process of computing the bias of  $\Psi$ .

In Sections 4 and 5.2, we empirically show the importance of accounting for the possible bias in both  $\Psi$  and OHT. Debiasing the  $\Psi$  field especially yields a considerable improvement on the latent  $\mathbf{v}$  field when we do not have direct observations to fit a model for  $\mathbf{v}$ .

*3.6. Complete OHT interpolation framework.* Algorithm 1 summarizes the full two-stage procedure we have described throughout this section. Procedures LGPR and DEBIAS summarize the proposed approximate EM algorithm and bias-correction as described in Sections 3.4 and 3.5, respectively. The computational complexity of our framework is dominated by the procedure LGPR, and thus is analogous to that of Kuusela and Stein (2018a). Given  $n_i$  observations for each year  $i = 1, \dots, I$ , the computational complexity of global Gaussian process regression is  $O(\sum_{i=1}^I n_i^3)$  due to computing the inverse Gram matrices  $\mathbf{K}_i^{-1}$ . The computation of LGPR is localized to  $|\mathcal{S}|$  target grid points at which the windows are centered, with each window containing  $w \cdot n_i$  observations for each year  $i$  ( $w$  is the fraction of data contained in the window). With the computations parallelized to  $C$  threads, the computational complexity of Algorithm 1 is  $O(P \cdot |\mathcal{S}| \cdot C^{-1} \cdot w^3 \cdot \sum_{i=1}^I n_i^3)$ .

**4. OHT Field Estimated from Argo Data.** In this section, we present empirical results applying the two-step estimation procedure described in Section 3 to the Argo dataset to produce output fields on a spatio-temporal grid  $\mathcal{X} \times \mathcal{T}$  where  $\mathcal{X}$  is a  $1^\circ \times 1^\circ$  spatial grid and  $\mathcal{T}$  is a regularly spaced monthly temporal grid centered on the 15th day of each month. Each quantity of interest is compared before and after applying the debiasing procedure described in Section 3.5. The bandwidth parameter  $\lambda_G$  for the spatial window is set to 442 km (approximately  $4^\circ$ ), and  $\lambda_t$  for the temporal window is set to 1.5 months. All computations in the subsequent sections are performed on Cheyenne (Laboratory, 2019), a high performance computing cluster at NCAR with 36 CPU nodes with 109 GB of RAM. It takes on average 25 min each to execute a single EM iteration and to make predictions on  $\mathcal{S}$  for each field.

In the subsequent Sections 4.1 and 4.2, we present the time-averaged quantities:

$$(17) \quad \text{Av}(\Upsilon)(\mathbf{x}) = \frac{1}{|\mathcal{T}|} \int_{\mathcal{T}} \mathbb{E}[\Upsilon(\mathbf{x}, \tau)] d\tau,$$

where  $\Upsilon$  can be  $\mathbf{v}$  or OHT depending on the context. Our product actually generates a monthly varying spatial map, however, we present time-averaged quantities which succinctly summarize spatial mean variability without loss of generality.

---

**Algorithm 1** Two-stage OHT interpolation framework
 

---

**Input:** Data  $\mathcal{D} = \{\mathcal{D}_1, \dots, \mathcal{D}_P\}$  where  $\mathcal{D}_p = \{(\theta_{ij}(p), \Psi_{ij}(p), \mathbf{s}_{ij}) : i = 1, \dots, I; j = 1, \dots, n_i\}$  (Denote  $\mathbf{s}_{\mathcal{D}} := \{\mathbf{s}_{ij} : \forall i, j\}$ ); Spatio-temporal target  $\mathbf{s}^*$

- 1: **function** LGPR( $\Upsilon, \mathcal{D}, \mathbf{S}$ ) ▷ Target response  $\Upsilon$  can be  $\Psi$  or OHT
- 2:     **repeat**
- 3:         Estimate mean field coefficients  $\widehat{\mathbf{B}}_{\Upsilon}$  in the (E-Step)
- 4:         Estimate covariance coefficients  $\widehat{\mathbf{\Xi}}_{\Upsilon}$  in the (M-Step)
- 5:     **until** Converge
- 6:     **return**  $\widehat{\Upsilon}(\mathbf{S})$  field
- 7: **end function**
  
- 8: **procedure** DEBIAS( $\Upsilon, \mathcal{D}, \widehat{\mathbf{\Xi}}_{\Upsilon}$ )
- 9:     Compute the bias  $\widehat{B}$  with (15).
- 10:    Debias  $\widehat{\Upsilon}$  and  $\widehat{\nabla_{\mathbf{x}} \Upsilon}$ , respectively, using  $\widehat{B}$  and (16).
- 11:    Re-estimate  $\widehat{\mathbf{\Xi}}_{\Upsilon}$  with (M-Step) using the bias-corrected residuals.
- 12:    Update  $\widehat{\Upsilon}$  field based on re-estimated  $\widehat{\mathbf{\Xi}}_{\Upsilon}$ .
- 13: **end procedure**
  
- 14: Estimate pilot predictions  $\widehat{\Psi}(\mathbf{s}_{\mathcal{D}}, p) \leftarrow \text{LGPR}(\Psi, \mathcal{D}_p, \mathbf{s}_{\mathcal{D}})$  for fine grid of  $p$ .
- 15: DEBIAS( $[\widehat{\Psi} - \widehat{m}_{\Psi}](\mathbf{s}_{\mathcal{D}}, p), \mathcal{D}_p, \widehat{\mathbf{\Xi}}_{\Psi}$ ) for fine grid of  $p$ .
- 16: Construct a dataset  $\widetilde{\mathcal{D}}$  whose response variable is predicted OHT,  $\widetilde{\text{OHT}}(\mathbf{s}_{\mathcal{D}})$ , using (11).
- 17: Map  $\widehat{\text{OHT}}(\mathbf{s}^*) \leftarrow \text{LGPR}(\widetilde{\text{OHT}}, \widetilde{\mathcal{D}}, \mathbf{s}^*)$ .
- 18: DEBIAS( $[\widehat{\text{OHT}} - \widehat{m}_{\text{OHT}}](\mathbf{s}^*), \widetilde{\mathcal{D}}, \widehat{\mathbf{\Xi}}_{\text{OHT}}$ ).

---

4.1. *Geostrophic Velocity*  $\hat{\mathbf{v}}$ . Recall from Section 3.3 that we only need spot-predicted velocities  $\mathbf{v}$  from the first step; however, it is worthwhile to visualize the interpolated latent  $\mathbf{v}$  field to see if the latent field is well-represented. The estimated mean field for the relative geostrophic velocity  $\text{Av}(\hat{\mathbf{v}}_{\text{rel}})$  from the first step can be found in Figure 4. Figures 4a and 4b show the non-bias-corrected initial zonal and meridional velocity estimates, respectively. Figures 4c and 4d show the estimated mean field after the debiasing procedure. In all figures, we mask out  $\pm 2^\circ$  equatorial bands, where geostrophic balance is invalid. The estimates depict the major ocean currents in each basin, including Equatorial Currents, the Antarctic Circumpolar Current, and (at least partially) the western boundary currents and their extensions. The debiasing procedure captures higher-order local features that are not described by the local second degree polynomial, without introducing spurious noise. This is highlighted in the Kuroshio Current (off the coast of Japan) and the Agulhas Return Current (near the southern tip of Africa), where meanders are clearly visible in Panel (d) that are not present in Panel (b) before the bias is corrected. These meanders are known to be quasi-stationary and are also observable in satellite products (see Section F of Supplementary Material), which indicates that these local features are in fact part of the real signal.

Even though we have only presented the velocity field estimated at 10 dbar in Figure 4, we emphasize that the relative velocity field is estimated at 17 different pressure levels. The vertical structure of the resulting velocity estimate is illustrated in Figure 5. Note that the relative velocity field in the continent-free Southern Ocean retains much of its strength even at 800 dbar, as opposed to the other basins, where the relative geostrophic velocities generally decay more quickly with depth.

4.2. *Heat Transport*  $\widehat{\text{OHT}}$ . Figure 6 shows the estimated mean field of zonal and meridional heat transport  $\text{Av}(\widehat{\text{OHT}})$  between 10 dbar to 900 dbar computed using the two-step procedure in Section 3.3. The heat transport fields largely resemble the geostrophic velocity

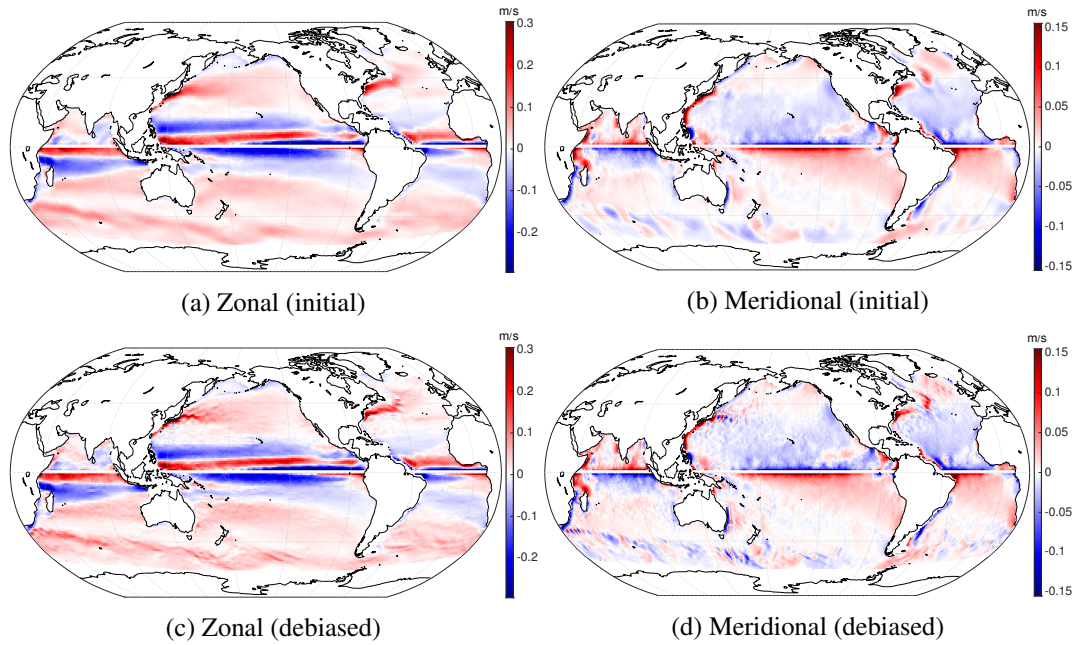


Fig 4: Estimated mean geostrophic velocity  $A_v$  ( $\hat{v}_{rel}$ ) at 10 dbar relative to 900 dbar. Red/blue corresponds to the east/west direction in the zonal quantities and north/south direction in the meridional quantities for every map figure here and below.

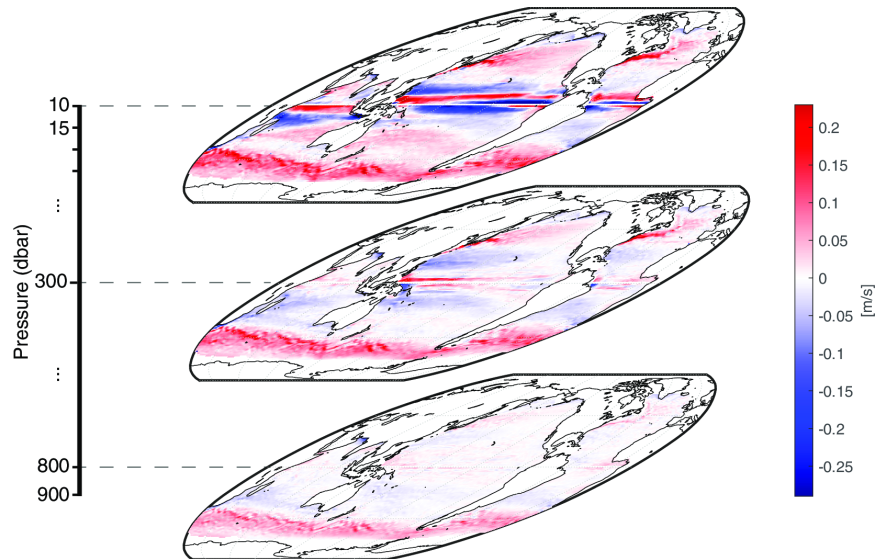


Fig 5: Estimated mean zonal velocities at multiple pressure levels (10, 300 and 800 dbar) .

fields, although temperature-driven features are noticeable in Figure 6. In addition, the vertical structure of the currents has a significant impact on these vertically integrated estimates. For instance, the Antarctic Circumpolar Current in the Southern Ocean becomes much more evident in the OHT estimate than it is in the velocity estimates, consistent with its role as the strongest, most depth-independent current in the global ocean. On the contrary, heat transport in the tropical Pacific does not stand out in Figure 6, even as the velocities in this region

dominate the near-surface flow shown in Figure 4. The varying contributions to the total OHT from transport in different depth layers can only be seen by resolving the vertical structure of the flow, as done in this work.

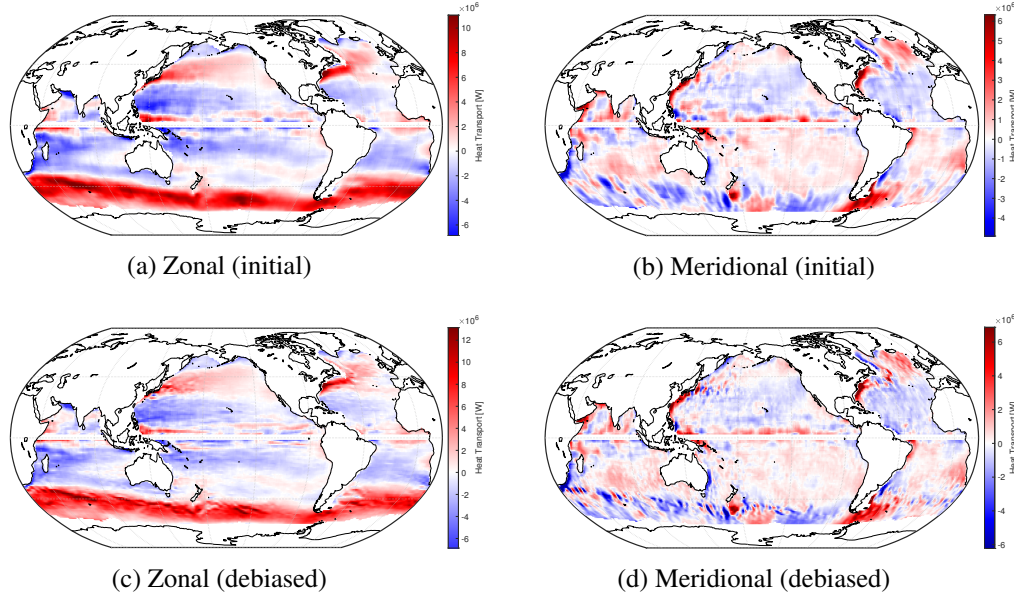


Fig 6: Estimated mean heat transport  $\overline{Av}(\widehat{OHT})$  between 10 dbar to 900 dbar.

**4.3. Heat Transport Anomalies and El Niño-Southern Oscillation.** The previous two sections illustrate the time-averaged mean fields, which by themselves are important for spatially resolving the global heat transport. In this section, we show the utility of quantifying the spatio-temporal OHT anomalies in the context of the El Niño-Southern Oscillation (ENSO), an important recurring phenomenon in the climate system.

ENSO is a natural mode of climate variability that influences Earth’s hydrological cycle and global weather patterns through teleconnections. ENSO alternates between a warm phase (El Niño) and a cold phase (La Niña), which are associated with changes in atmospheric circulation and ocean temperature. The state and intensity of ENSO can be described using NOAA’s Oceanic Niño Index (ONI, [Glantz and Ramirez, 2020](#)), which is a 3-month running mean of ERSST.v5 Sea Surface Temperature (SST) anomalies in the east-central tropical Pacific between  $5^{\circ}\text{N}$ – $5^{\circ}\text{S}$ ,  $120^{\circ}$ – $170^{\circ}\text{W}$  (El Niño 3.4 region). An event is classified as an El Niño (La Niña) when ONI is above (below) the threshold of  $\pm 0.5^{\circ}\text{C}$  for a minimum of 5 consecutive overlapping seasons. See Figure 7, Panel (B) for a time series of the ONI.

Figure 7 shows Hovmöller diagrams of the OHT anomaly across latitude and time. We present the total heat anomaly transported across the longitudes of the Niño 3.4 region for meridional OHT (Panel A), whereas the anomaly averaged over all longitudes of the Niño 3.4 region is presented for zonal OHT (Panels C1–C3). Panel A and Panel C1 provide a kinematic view of anomalous heat transport in the upper ocean between 10–100 dbar. The El Niño phase is associated with anomalous meridional transport of heat away from the Equator (red / blue in Northern / Southern hemisphere in Panel A) and dominant eastward anomalous heat transport (red in Panel C1), and vice versa for the La Niña phase. These observations are consistent with our scientific understanding of ENSO. During El Niño conditions, the normal

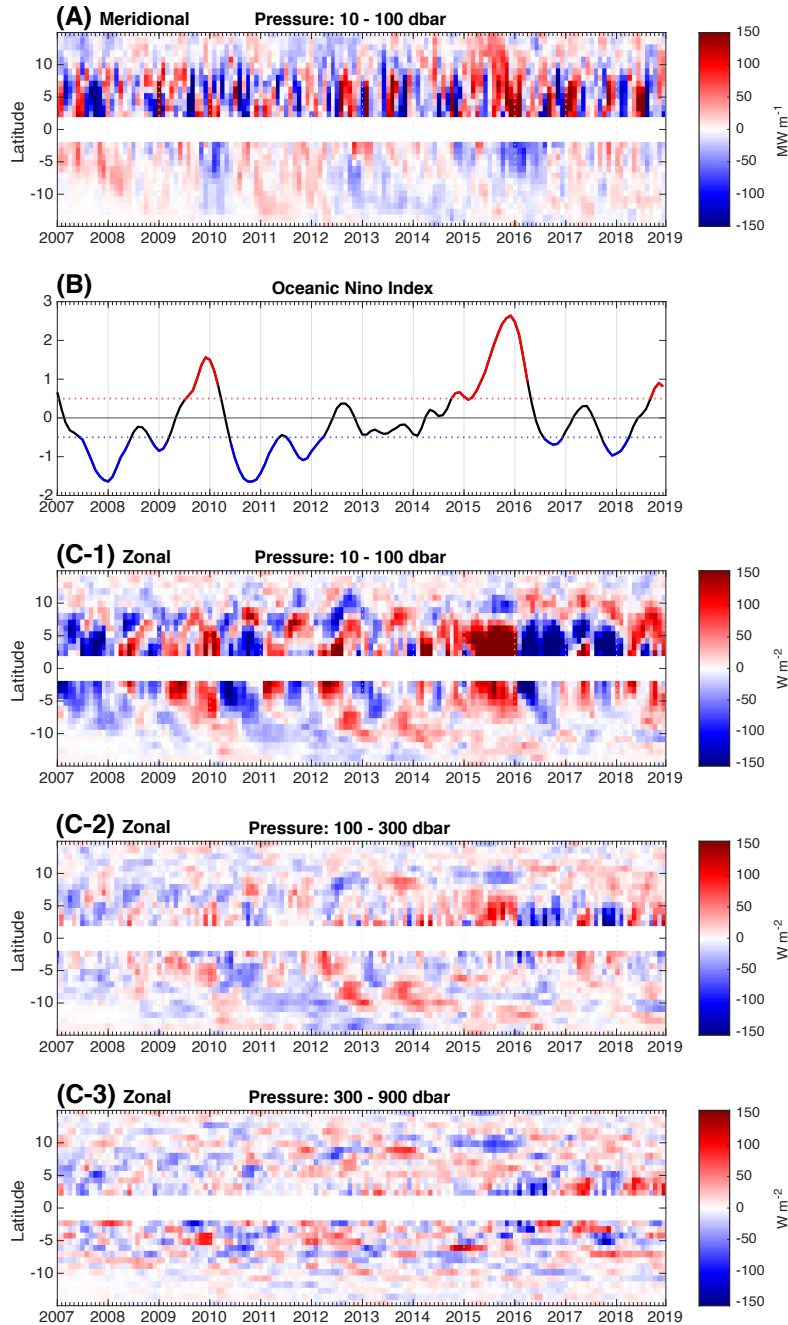


Fig 7: Ocean heat transport anomaly over the longitude band of El Niño 3.4 region has a close connection to the Oceanic Niño Index. Panel (A): Total meridional heat transport anomaly at the 10–100 dbar pressure range. Red/blue means north/south direction. Panel (B): Historical ONI. Panels (C): Averaged zonal heat transport anomaly for pressure layers 10–100 dbar, 100–300 dbar, and 300–900 dbar (from top to bottom). Red/blue means east/west direction.

upwelling of cold waters along the equator is reduced, yielding upper ocean temperatures that are warmer than average, while increased upwelling in the La Niña phase results in cooler waters in the surface layer of the tropical Pacific (McPhaden, Santoso and Cai, 2020). Furthermore, variations in anomalous upper-ocean currents have been observed during the

development of ENSO. Ren et al. (2017) found that, at the equator, eastward (positive) zonal current anomalies strengthened in early 2015 before the anomalous currents turned to the west (negative) by 2016, in general agreement with the estimate presented in Panel C1.

From Panels C1–C3, we can observe that the anomalous heat transport associated with ENSO occurs predominantly in the upper layer of the ocean and that the patterns are subdued in the deeper parts of the ocean, which matches with earlier studies of ocean heat content variability (see, e.g., Trenberth et al., 2016). During the 2015–16 super El Niño episode, the strongest El Niño in history, the anomalous zonal heat transport exhibits a coherent pattern that extends to the deeper 100–300 dbar layer. Compared to conventional indices or the rate of change in ocean heat content (Trenberth et al., 2016), Figure 7 reveals intriguing, complex spatial variability (the study of which remains outside the scope of this paper). For example, the meridional component of the anomalous heat transport has a much larger inter-hemispheric asymmetry than does the zonal component.

**5. Validation with Satellite Observations.** In this section, we provide empirical validation of our method and the resulting estimates by comparing with estimates based on satellite observations. The ultimate goal of the validation is to show our estimates align well with the existing products widely used by the oceanographic community, and ascertain the strength of the proposed method, i.e, the two-stage procedure together with the debiasing procedure.

Satellite data offer an excellent tool for validating our gridded near-surface OHT estimates, as satellites capture high-resolution snapshots of SST and sea surface height (SSH, which can be used to estimate geostrophic velocity at the surface). Higher resolution is a clear advantage of satellite observations compared to sparse in-situ data collected from research vessels, Argo floats, and moorings; in-situ subsurface measurements are, however, crucial for characterizing OHT over the depth of the water column, as in Definition (1). In this section, we use the *surface temperature transport*  $TT_0(\mathbf{s}) = \theta(\mathbf{s}, z_0)\mathbf{v}(\mathbf{s}, z_0)$  instead of OHT, with  $z_0$  equal to 0 dbar for satellite based products (which are available only at the surface) and 10 dbar for our Argo-based in-situ product (the shallowest depth we considered). Using  $TT_0(\mathbf{s})$  instead of OHT, which corresponds to ignoring terms that do not impact the comparison, allows us to leverage observations available from satellites for validation analysis.

We adopted two separate satellite gridded products for SST and SSH distributed by the EU Copernicus Marine Environment Monitoring Service (CMEMS). For SST, the European Space Agency (ESA) SST Climate Change Initiative (CCI) and Copernicus Climate Change Service (C3S) reprocessed Level-4 product (Merchant et al., 2019) at daily  $0.05^\circ$  degree spatial resolution is considered. For SSH and its derived geostrophic velocity, sea level TAC-DUACS Level-4 Delayed-Time product (Taburet et al., 2019) is adopted. This product has a quarter-degree spatial resolution, along with daily temporal resolution. The DUACS product contains state-of-the-art surface geostrophic velocity estimates mainly based on multimission satellite altimetry over the global ocean, although in-situ Argo profiles and surface drifters are also used in part to estimate the Mean Dynamic Topography (Rio et al., 2018). However, the impact of in-situ observations on the DUACS product is negligible in validating the proposed framework and the estimates from Argo data.

**5.1. Comparing the OHT pipelines.** The primary reason we propose a two-stage method is that Argo floats do not directly measure velocity. Such a limitation requires us to first estimate the velocity and then combine the resulting estimates with in-situ temperature observations before interpolating in any space and time coordinates. The performance of the proposed procedure therefore depends on both the velocity estimation error and the OHT mapping error. Using the satellite-based SST and SSH products, we separately analyze the errors associated with each of these components.

The first step is to establish the *ground truth*, defined here as the best possible gridded surface temperature transport field at  $1^\circ \times 1^\circ$  spatial resolution. For this purpose, we compute the product of the gridded SST and velocity fields at  $0.25^\circ \times 0.25^\circ \times 1$  day resolution and then upscale the result to the target resolution using natural-neighbor interpolation (Sibson, 1981). This upscaled *ground truth* is not influenced by any of our proposed interpolation methods. See Section F of the Supplementary Material (Park et al., 2020) for the resulting ground truth time-averaged  $\widehat{\text{TT}}_0$  field.

A key advantage of utilizing high-resolution satellite products is that we can obtain SST ( $\theta$ ), SSH<sup>2</sup> ( $\Psi$ ), and velocity ( $\mathbf{v}$ ) in any spatio-temporal location up to the resolution each product can resolve. We generated *pseudo-observations*  $\mathcal{D}_{\text{Pseudo}} = \{(\theta(\mathbf{s}_{ij}), \Psi(\mathbf{s}_{ij}), \mathbf{v}(\mathbf{s}_{ij})) : \mathbf{s}_{ij} \in \mathcal{s}_{\mathcal{D}}, \forall i, j\}$  at the same spatio-temporal locations as the Argo array  $\mathcal{s}_{\mathcal{D}}$  by taking the nearest high-resolution spatio-temporal grid point of SST, SSH, and velocity, respectively. Since the nearest high-resolution grid-point from any observed locations in  $\mathcal{s}_{\mathcal{D}}$  is at most  $0.177^\circ \times 0.5$  days away, the approximation error is marginal in comparison to the sampling resolution of the Argo array. By construction, these pseudo-observations match the sampling resolution; hence, surface temperature transport estimates derived from in-situ Argo profiles and from pseudo-observations are commensurable, allowing us to assess our method in comparison to the *ground truth*.

We consider three candidate methods  $\mathcal{M}_j, j \in \{1, 2, 3\}$  to estimate the surface temperature transport field  $\widehat{\text{TT}}_0(\mathbf{s}^*)$  as follows:

$$\mathcal{M}_1 : \widehat{\theta} \cdot \widehat{\mathbf{v}}(\mathbf{s}^*), \quad \mathcal{M}_2 : \widehat{\theta} \cdot \widehat{\widehat{\mathbf{v}}}(\mathbf{s}^*), \quad \mathcal{M}_3 : \widehat{\theta}(\mathbf{s}^*) \cdot \widehat{\mathbf{v}}(\mathbf{s}^*)$$

where  $\widehat{(\cdot)}(\mathbf{s}^*)$  is used to denote the estimate of  $(\cdot)$  at any spatio-temporal point  $\mathbf{s}^*$  given the data  $\mathcal{D}_{\text{Pseudo}}$ . Our proposed procedure from Section 3.3 corresponds to  $\mathcal{M}_2$ , where we estimate  $\mathbf{v}$  from  $\Psi$  and interpolate the  $\widehat{\text{TT}}_0$  field based on the in-situ  $\widehat{\theta} \cdot \widehat{\mathbf{v}}$ . All results hereafter are based on estimates after debiasing on all stages.

$\mathcal{M}_1$  is a hypothetical procedure where we assume that  $\mathbf{v}$  can be obtained without estimation which is not feasible in practice (except at the surface where we have access to satellite-based  $\mathbf{v}$  fields). Given  $\mathcal{D}_{\text{Pseudo}}$ ,  $\mathcal{M}_1$  only requires a second stage procedure that reduces to the local Gaussian process method from Kuusela and Stein (2018a). Thus, the performance of  $\mathcal{M}_1$  signifies the idealized interpolation capability of the local Gaussian process method when sparse spatio-temporal measurements are fully observed. Meanwhile,  $\mathcal{M}_3$  is an alternative approach detailed in Appendix A, where the two gridded products  $\widehat{\theta}$  and  $\widehat{\mathbf{v}}$  can only be accessed separately. Such a situation frequently arises in oceanographic data analysis, in which case this approach is deemed a conventional norm. In this scenario, two separate interpolations—one for  $\theta$  and the other for  $\mathbf{v}$ —are needed; OHT is computed as the product of the two gridded fields.

Figure 8 shows the calibration between the time-averaged surface temperature transport field  $\text{Av}(\widehat{\text{TT}}_0)$  on a  $1^\circ \times 1^\circ$  spatial grid computed with the three methods  $\mathcal{M}_1, \mathcal{M}_2, \mathcal{M}_3$  and the ground truth.  $\mathcal{M}_1$  (in blue) clearly performs the best of the three competing models, as the velocity  $\mathbf{v}$  is fully observed in this case (i.e., the first stage estimation achieves zero error). Note that estimating the meridional OHT is an intrinsically harder problem than estimating the zonal OHT. This asymmetry most likely stems from the fact that across most of the open ocean, the meridional signal is substantially smaller than the zonal signal (Zheng and Giese, 2009; Forget and Ferreira, 2019), leading to a decrease in the signal-to-noise ratio.

<sup>2</sup>Although SSH and dynamic height anomaly are not the same, in this section we also use  $\Psi$  to denote SSH, with abuse of notation, since they fulfill the same purpose here.

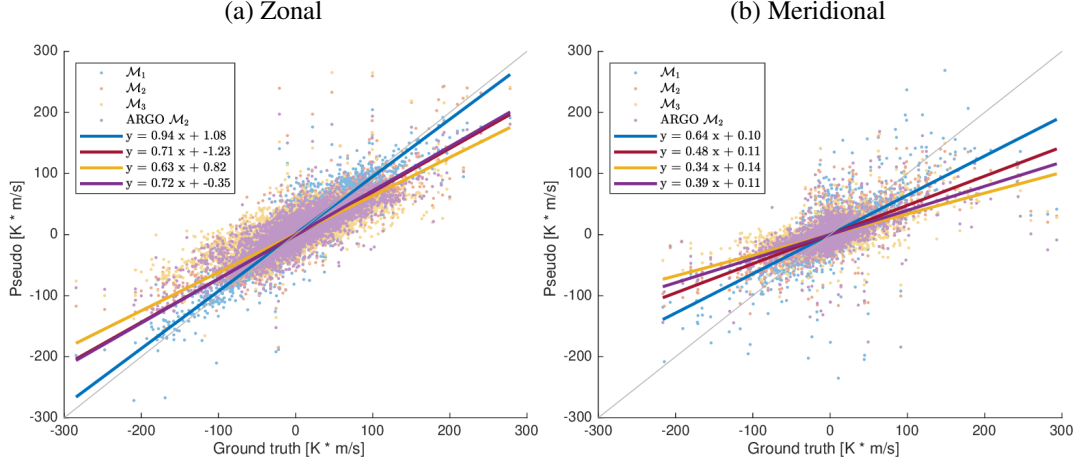


Fig 8: Calibration of time-averaged zonal and meridional surface temperature transport  $\text{Av}(\text{TT}_0)$  on  $1^\circ \times 1^\circ$  spatial grid between ground truth and competing models. For each case, the estimated regression line is superimposed with the same color.

TABLE 1  
Prediction performance of  $\text{TT}_0$  estimation methods.

		$\mathcal{M}_1$	$\mathcal{M}_2$	$\mathcal{M}_3$	Argo $\mathcal{M}_2$
Zonal	RMSE	38.3	40.8	53.5	41.3
	MAD	4.12	4.23	4.25	4.28
	MIGN	4.63	4.66	4.79 <sup>†</sup>	4.71
	MCRPS	12.5	12.5	14.9 <sup>†</sup>	12.9
Meridional	RMSE	37.1	38.4	42.6	39.1
	MAD	4.01	4.09	4.11	4.12
	MIGN	4.58	4.61	4.66 <sup>†</sup>	4.69
	MCRPS	11.9	12.0	13.1 <sup>†</sup>	12.0

<sup>†</sup> Based on an approximation.

Under a more realistic regime where  $\mathbf{v}$  cannot be directly observed, the proposed two-stage procedure  $\mathcal{M}_2$  outperforms  $\mathcal{M}_3$  by leveraging the high-frequency signals maintained from the first stage, in terms of both better calibration to the ground truth (Figure 8) and four quantitative performance measures—root mean squared error (RMSE), median absolute deviation (MAD), median ignorance score (MIGN, Roulston and Smith, 2002), and median continuous ranked probability score (MCRPS, Gneiting, Balabdaoui and Raftery, 2007)—as seen in Table 1. The performance metrics for  $\Upsilon$  are calculated as follows:

$$\text{RMSE} = \sqrt{\frac{1}{|\mathcal{S}|} \sum_{s \in \mathcal{S}} \left( \Upsilon_{\text{GT}}(s) - \hat{\Upsilon}(s) \right)^2}, \quad \text{MAD} = \text{Med}_{s \in \mathcal{S}} \left| \Upsilon_{\text{GT}}(s) - \hat{\Upsilon}(s) \right|,$$

$$\text{MIGN} = \text{Med}_{s \in \mathcal{S}} \left[ -\log p(\Upsilon_{\text{GT}}(s) \mid \mathcal{D}; \hat{\mathbf{B}}, \hat{\mathbf{\Xi}}) \right],$$

$$\text{MCRPS} = \text{Med}_{s \in \mathcal{S}} \int \left[ F(\Upsilon \mid \mathcal{D}; \hat{\mathbf{B}}, \hat{\mathbf{\Xi}}) - \mathbb{1}(\Upsilon \geq \Upsilon_{\text{GT}}(s)) \right]^2 d\Upsilon,$$

where  $\Upsilon_{\text{GT}}$  is the ground truth field,  $p(\cdot \mid \mathcal{D})$  and  $F(\cdot \mid \mathcal{D})$  are the predictive probability density function and predictive cumulative distribution function, respectively. While RMSE

and MAD primarily assess the deterministic accuracy of the predictions, MIGN and MCRPS measure the probabilistic accuracy by taking both the deterministic accuracy and precision into consideration. MIGN measures the goodness of fit of the predictive distribution to the ground truth, and MCRPS can be viewed as a generalized version of MAD (Gneiting, Balabdaoui and Raftery, 2007). The predictive distribution of  $\mathcal{M}_1$  and  $\mathcal{M}_2$  is Gaussian with analytically tractable mean and variance; however, that of  $\mathcal{M}_3$  is no longer Gaussian and entails further approximations for computing the MIGN and MCRPS since the estimate is the product of two correlated Gaussian random variables. Here MIGN and MCRPS for  $\mathcal{M}_3$  are computed using an approximate predictive distribution assuming that  $\hat{\theta}$  and  $\hat{v}$  are jointly Gaussian. The reported values do not change up to 3 significant digits when varying the correlation from  $-1$  to  $1$ .

In addition to validating the two-stage procedure, comparing the surface temperature transport estimates derived from in-situ Argo profiles  $\mathcal{D}$  to those constructed from the pseudo observations  $\mathcal{D}_{\text{pseudo}}$  further confirms that the results presented in Section 4 are optimal in terms of the proposed framework. In Figure 8, Table 1, we provide the calibration and point prediction performance of the Argo-based estimate (denoted as Argo  $\mathcal{M}_2$  to emphasize that  $\mathcal{M}_2$  is comparable) with reference to the ground truth. The estimates derived from actual Argo profiles are surprisingly close to those based on pseudo observations ( $\mathcal{M}_2$ ) and outperform  $\mathcal{M}_3$ . A performance degradation between Argo  $\mathcal{M}_2$  and  $\mathcal{M}_2$  could arise mainly for two possible reasons: (A) Argo-based estimates are computed at a near surface pressure (10 dbar) unlike the ground truth and  $\mathcal{M}_2$  estimates, and (B) reference velocities at 900 dbar adopted from Gray and Riser (2014) might be underestimated. The good agreement found here demonstrates that these effects are minor in comparison to the other factors contributing to the overall performance of our method.

Recall that  $\mathcal{M}_1$  is the idealized estimate when  $\mathbf{v}$  is perfectly known. In other words, if we could improve our  $\mathbf{v}$  estimate in the first stage, we might be able to achieve performance close to  $\mathcal{M}_1$  even with in-situ Argo profiles alone. One can consider a natural extension of this work that synthesizes the high-resolution satellite product with the in-situ Argo profile dataset (Rio and Santoleri, 2018), which is an interesting direction for future improvement but well beyond the scope of the present study. Our results do emphasize, however, that the coarse sampling resolution is the main cause of miscalibration in comparison to the satellite-based ground truth. The miscalibration arises mostly near western boundaries and in regions with sharp fronts, where abrupt changes occur and strong currents are present. These issues could be explained by (A) the innate bias incurred from the nonparametric regression approach and/or (B) the inability of the Argo fleet to sample the coastal shelves, where the floats cannot reach 2000 dbar. There have been numerous methods proposed in the statistics literature to reduce the innate bias of (A). We tried the non-local means (Arias-Castro, Salmon and Willett, 2011) and concluded that the method brings a marginal improvement in identifying the fronts. On the other hand, in Section H of the Supplementary Material (Park et al., 2020), we confirmed that including Spray glider observations (Sherman et al., 2001; Rudnick, 2016) mitigates the underestimation occurring in the narrow boundary current in the western North Atlantic. These results indicate that the miscalibration stems more from the Argo array’s sampling deficiencies in the coastal regions and highly variable boundary currents and less from a boundary bias due to the nonparametric regression approach.

*5.2. Effect of Debiasing Procedure.* In this section, we discuss the efficacy of the debiasing procedure proposed in Section 3.5. Figure 9 and Table 2 give the point prediction performance of the debiasing procedure on the first stage. Both show that the debiasing procedure improves the mapping of both zonal and meridional velocities. Notice that the local interpolation procedure yields a globally calibrated SSH ( $\Psi$ ) field (Figure 9a) as compared

to the  $\mathbf{v}$  field (Figure 9b,9c). While not surprising, this does demonstrate that predicting the gradient field from unobserved  $\mathbf{v}$  is a harder problem than estimating the underlying  $\Psi$  field itself. This result also implies that the procedure may smooth more than the actual curvature in regions where sharp magnitude changes occur in the  $\Psi$  field. Choosing a smaller bandwidth parameter may alleviate this concern but leads to unstable estimates because fewer observations are then available within each local spatio-temporal window. A data-driven bandwidth selector would be an appealing refinement (Fan and Gijbels, 1995; Ruppert and Wand, 1994; De Brabanter et al., 2013). However, the associated improvements are known to be inconsistent depending on the data, not to mention that our current concern lies mainly in the derivative estimation, rather than estimating the observable response  $\Psi$ .

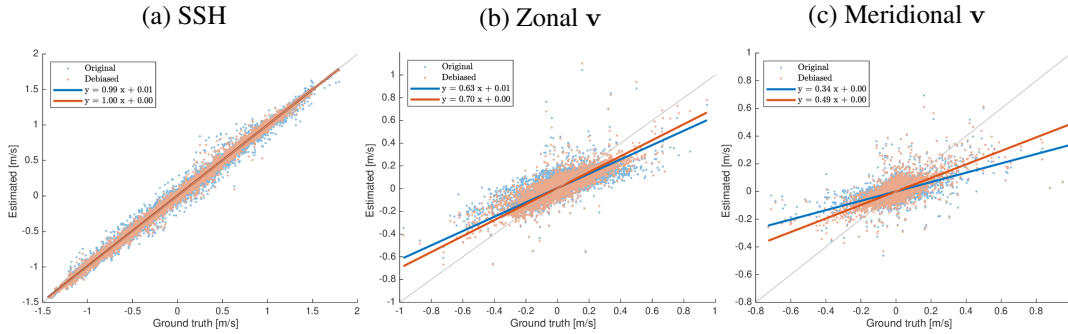


Fig 9: Calibration of time-averaged  $\Psi$  and  $\mathbf{v}$  between ground truth and estimates, respectively, with and without debiasing.

TABLE 2

Point prediction performance of  $\text{Av}(\hat{\mathbf{v}})$  by the debiasing procedure regarding RMSE, MAD, and correlation  $\rho$ . The best results are highlighted in bold.

	Zonal		Meridional	
	Without Debias	Debias $\Psi$	Without Debias	Debias $\Psi$
RMSE	0.059	<b>0.047</b>	0.046	<b>0.039</b>
MAD	0.018	<b>0.015</b>	0.012	<b>0.010</b>
$\rho$	0.781	<b>0.873</b>	0.536	<b>0.708</b>

Figure 10 and Table 3 show the calibration and point prediction performance of the debiasing procedure within the two-stage procedure. We separated out the debiasing efficacy based on whether we only debias  $\Psi$  but not  $\text{TT}_0$ , debias  $\text{TT}_0$  without debiasing  $\Psi$ , or debias both  $\Psi$  and  $\text{TT}_0$ . The result indicates that both estimates should be debiased in order to fully leverage the potential that the debiasing procedure can deliver. Notice that debiasing at the second stage is crucial for the performance gain. Only debiasing the first stage leaves an inconsistent result, even though the procedure does improve velocity prediction in the first stage as seen in Figure 9 and Table 2. Both phenomena can be understood from the fact that the numerical magnitude of the temperature  $\theta$  is much greater than that of the velocity  $\mathbf{v}$ . The correction accounting for the larger magnitude, i.e., temperature  $\theta$ , should play the biggest role in accurate prediction of the final  $\text{TT}_0$  field. Meanwhile, this also implies that a slight perturbation in  $\mathbf{v}$ , whose magnitude is small, may introduce a large deviation in  $\text{TT}_0$  when multiplied with  $\theta$ . Without debiasing the  $\text{TT}_0$  in the second stage, predictions made with only the first stage correction are likely to yield subpar performance.

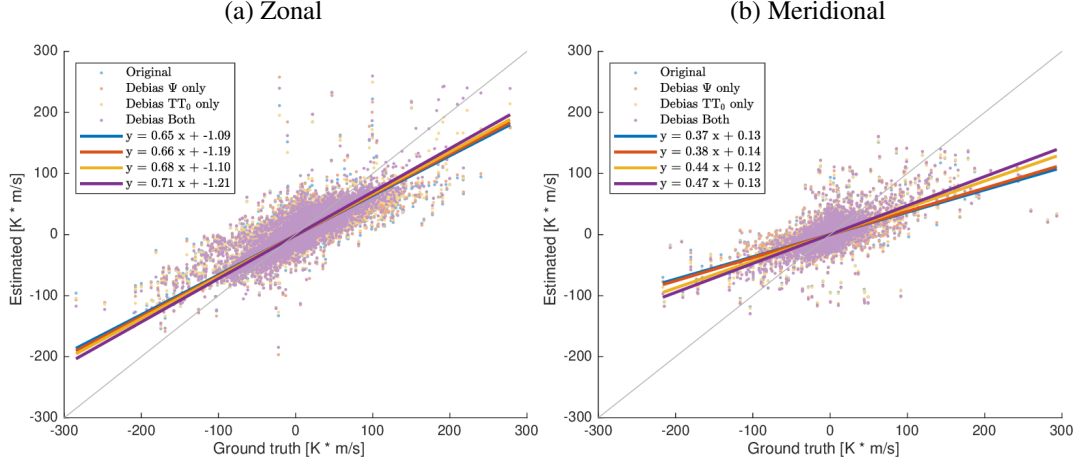


Fig 10: Calibration of time-averaged surface temperature transport  $\overline{TT}_0$  between ground truth and estimates, depending on which debiasing procedures are applied.

TABLE 3  
Point prediction performance of  $\widehat{Av}(\overline{TT}_0)$  by the debiasing procedure regarding RMSE, MAD, and correlation  $\rho$ . The best results are highlighted in bold.

		Without Debias	Debias $\Psi$ only	Debias $\overline{TT}_0$ only	Debias both
Zonal	RMSE	16.41	16.38	14.81	<b>14.30</b>
	MAD	5.653	5.688	5.260	<b>5.164</b>
	$\rho$	0.811	0.809	0.854	<b>0.862</b>
Meridional	RMSE	12.71	12.71	11.53	<b>11.22</b>
	MAD	3.281	3.309	3.161	<b>3.160</b>
	$\rho$	0.588	0.590	0.680	<b>0.700</b>

**6. Discussion and Conclusions.** In this paper, we introduced a comprehensive spatio-temporal interpolation framework for estimating the global ocean heat transport using in-situ Argo profiles. The framework characterizes a partially observed OHT process as well as the latent velocity process  $\mathbf{v}$  represented by the gradient of an observed quantity, both of which are spatio-temporally correlated in a heterogeneous fashion. Our contributions to OHT estimation are threefold: we formalize the statistical challenges as an end-to-end latent LGPR model accompanied by the two-stage estimation procedure, introduce the approximate EM procedure for jointly estimating both the mean and the covariance parameters, and refine the potentially misspecified mean field model with the debiasing procedure. Our data-driven interpolated fields are on par with state-of-the-art multimission satellite products near the surface, at the spatial resolution that Argo can resolve, and yield sensible new subsurface OHT estimates that can provide useful insights into crucial scientific phenomena.

Even though our comprehensive framework was targeted at quantifying ocean heat transport, the techniques involved resonate with broader statistical issues, enabling possible extensions and raising interesting questions that we have not fully addressed in this paper. For example, we handle the latent gradient field by adopting the local Gaussian process. However, nonparametric *derivative estimation* has a long-standing history in statistics with contributions characterizing the optimal derivative estimator based on various criteria as well as data-driven methods to choose the optimal tuning parameters (Charnigo, Hall and Srinivasan, 2012; Wang and Lin, 2015; Dai, Tong and Genton, 2016; Liu and De Brabanter, 2018). Most existing literature on derivative estimation considers a univariate covariate, and extending the

established results to the spatio-temporal case is not trivial as spatial local regression itself requires substantial theoretical considerations (Hallin, Lu and Tran, 2004).

Another interesting direction is jointly modeling the temperature and velocity fields based on the underlying process for temperature and salinity. Dynamic height anomaly, modeled separately from temperature in this work, is indeed a nonlinear function of temperature and salinity, which are the primitive measurements we obtain from the Argo floats. An exciting extension of our approach could be modeling the temperature and dynamic height anomaly fields instead as a bivariate Gaussian process, similar to the approach taken by Yarger, Stoev and Hsing (2020) for jointly modeling temperature and salinity. Admittedly, finding an appropriate cross-correlation function between temperature and dynamic height anomaly might not be as straightforward as for temperature and salinity.

While we relied on the local Gaussian process to define the spatio-temporal process, the complete characterization of the second order structure (covariance kernel) is not enough to describe the full process when it is non-Gaussian. Even commonly used climate variables, such as temperature, are known to show non-Gaussian properties (Kuusela and Stein, 2018a; Stein, 2019). It could therefore be possible to explore non-Gaussian models (e.g., Bolin and Wallin, 2020) to improve the prediction of the spatio-temporal process.

Vertical dependence, i.e., correlation across pressure levels, is an important aspect of any profile measurements, including the  $T$ - $S$  profiles. The dynamic height anomaly  $\Psi$  has an additional interesting property in that it is a monotonically increasing function of depth by definition. While our approach partially accommodates the vertical structure, the vertical dependence is not fully modeled. Completely accounting for the vertical structure would yield several improvements, including a truly four-dimensional map of global ocean heat transport, effective confinement of the random fields with respect to depth using the monotonicity condition, and a complete uncertainty quantification of the OHT field. Yarger, Stoev and Hsing (2020) proposed functional PCA as a way of handling the vertical dependence, even though their focus was on modeling temperature and salinity where the monotone constraint is not required. Fully characterizing the vertical dependence of the global ocean circulation and associated OHT is additionally of great interest to the oceanographic community and thus represents a priority for future work.

**Acknowledgements.** We would like to acknowledge high-performance computing support from Cheyenne (doi:10.5065/D6RX99HX) provided by NCAR’s Computational and Information Systems Laboratory, sponsored by the National Science Foundation. Donata Giglio acknowledges support from NSF (Award 2026954) and NASA (Award NNX20ZDA001N-PO). Alison Gray acknowledges support from NASA (Award NNX80NSSC19K1252), the U.S. Argo Program through NOAA (Award NA15OAR4320063), and the Microsoft Faculty Fellowship program. We are grateful to the Statistical Oceanography and STAMPS groups, and especially to Fred Bingham, Sarah Gille and Matt Mazloff for constructive discussions and suggestions related to Argo, Spray data and physical oceanography. We appreciate the constructive feedback by the Editor, the Associate Editor and the two anonymous reviewers which substantially improved the utility and readability of the paper.

## SUPPLEMENTARY MATERIAL

**Supplement A: Supplement to “Spatio-temporal Local Interpolation of Global Ocean Heat Transport using Argo Floats: A Debiased Latent Gaussian Process Approach”**

(doi: COMPLETED BY THE TYPESETTER; .pdf). We provide in the supplement additional details on quality control, analytic formulas regarding the covariance kernel, explicit derivations of the EM procedure, the predictive distribution for single depth OHT, and supporting figures, as well as extensive additional analyses where Spray glider profiles are jointly analyzed with Argo float profiles.

## REFERENCES

- ARGO (2020). Argo float data and metadata from Global Data Assembly Centre (Argo GDAC). DOI: 10.17882/42182.
- ARIAS-CASTRO, E., SALMON, J. and WILLET, R. (2011). Oracle inequalities and minimax rates for non-local means and related adaptive kernel-based methods. *arXiv:1112.4434 [cs, math, stat]*. arXiv: 1112.4434.
- BANERJEE, S., GELFAND, A. E. and SIRMANS, C. F. (2003). Directional Rates of Change Under Spatial Process Models. *Journal of the American Statistical Association* **98** 946–954.
- BARKER, P. M. and MCDUGALL, T. J. (2020). Two Interpolation Methods Using Multiply-Rotated Piecewise Cubic Hermite Interpolating Polynomials. *Journal of Atmospheric and Oceanic Technology* **37** 605–619.
- BAYARRI, M. J., WALSH, D., BERGER, J. O., CAFFEO, J., GARCIA-DONATO, G., LIU, F., PALOMO, J., PARTHASARATHY, R. J., PAULO, R. and SACKS, J. (2007). Computer model validation with functional output. *The Annals of Statistics* **35** 1874–1906.
- BEHRENS, E., FERNANDEZ, D. and SUTTON, P. (2019). Meridional Oceanic Heat Transport Influences Marine Heatwaves in the Tasman Sea on Interannual to Decadal Timescales. *Frontiers in Marine Science* **6** 228.
- BOLIN, D. and WALLIN, J. (2020). Multivariate type G Matérn stochastic partial differential equation random fields. *Journal of the Royal Statistical Society Series B* **82** 215–239.
- BRYDEN, H. L. and IMAWAKI, S. (2001). Chapter 6.1 Ocean heat transport. In *International Geophysics*, (G. Siedler, J. Church and J. Gould, eds.). *Ocean Circulation and Climate* **77** 455–474. Academic Press.
- BRYNJARSDÓTTIR, J. and O’HAGAN, A. (2014). Learning about physical parameters: the importance of model discrepancy. *Inverse Problems* **30** 114007. Publisher: IOP Publishing.
- CHARNIGO, R., HALL, B. and SRINIVASAN, C. (2012). A Generalized Cp Criterion for Derivative Estimation. *Technometrics*.
- LABORATORY, C. A. I. S. (2019). Cheyenne: SGI ICE XA Cluster. doi: 10.5065/D6RX99HX.
- CRESSIE, N. (1993). *Statistics for Spatial Data*, revised ed. John Wiley & Sons, New York.
- CRESSIE, N. and WIKLE, C. K. (2011). *Statistics for Spatio-Temporal Data*. John Wiley & Sons.
- CSISZAR, I. and TUSNADY, G. (1984). Information geometry and alternating minimization procedures. *Statistics and decisions* **1** 205–237. Publisher: Oldenburg Verlag.
- DAI, W., TONG, T. and GENTON, M. G. (2016). Optimal Estimation of Derivatives in Nonparametric Regression. *Journal of Machine Learning Research* **17** 1–25.
- DE BRABANTER, K., DE BRABANTER, J., DE MOOR, B. and GIJBELS, I. (2013). Derivative estimation with local polynomial fitting. *The Journal of Machine Learning Research* **14** 281–301.
- DEMPSTER, A. P., LAIRD, N. M. and RUBIN, D. B. (1977). Maximum Likelihood from Incomplete Data Via the EM Algorithm. *Journal of the Royal Statistical Society: Series B (Methodological)* **39** 1–22.
- FAN, J. and GIJBELS, I. (1995). Data-Driven Bandwidth Selection in Local Polynomial Fitting: Variable Bandwidth and Spatial Adaptation. *Journal of the Royal Statistical Society: Series B (Methodological)* **57** 371–394.
- FAN, J., GASSER, T., GIJBELS, I., BROCKMANN, M. and ENGEL, J. (1997). Local Polynomial Regression: Optimal Kernels and Asymptotic Minimax Efficiency. *Annals of the Institute of Statistical Mathematics* **49** 79–99.
- FORGET, G. and FERREIRA, D. (2019). Global ocean heat transport dominated by heat export from the tropical Pacific. *Nature Geoscience* **12** 351–354.
- FORGET, G. and PONTE, R. M. (2015). The partition of regional sea level variability. *Progress in Oceanography* **137** 173–195.
- FRITSCH, F. N. and CARLSON, R. E. (1980). Monotone Piecewise Cubic Interpolation. *SIAM Journal on Numerical Analysis* **17** 238–246.
- GANACHAUD, A. and WUNSCH, C. (2000). Improved estimates of global ocean circulation, heat transport and mixing from hydrographic data. *Nature* **408** 453–457. Number: 6811 Publisher: Nature Publishing Group.
- GLANTZ, M. H. and RAMIREZ, I. J. (2020). Reviewing the Oceanic Niño Index (ONI) to Enhance Societal Readiness for El Niño’s Impacts. *International Journal of Disaster Risk Science* **11** 394–403.
- GNEITING, T., BALABDAOUI, F. and RAFTERY, A. E. (2007). Probabilistic forecasts, calibration and sharpness. *Journal of the Royal Statistical Society: Series B (Statistical Methodology)* **69** 243–268.
- GOOD, S. A., MARTIN, M. J. and RAYNER, N. A. (2013). EN4: Quality controlled ocean temperature and salinity profiles and monthly objective analyses with uncertainty estimates. *Journal of Geophysical Research: Oceans* **118** 6704–6716.
- GRAY, A. R. and RISER, S. C. (2014). A Global Analysis of Sverdrup Balance Using Absolute Geostrophic Velocities from Argo. *Journal of Physical Oceanography* **44** 1213–1229.
- GRAY, A. R. and RISER, S. C. (2015). A method for multiscale optimal analysis with application to Argo data. *Journal of Geophysical Research: Oceans* **120** 4340–4356.
- GUERRIER, S., KAREMERA, M., ORSO, S. and VICTORIA-FESER, M.-P. (2020). Asymptotically Optimal Bias Reduction for Parametric Models. *arXiv:2002.08757 [math, stat]*. arXiv: 2002.08757.

- HAAS, T. C. (1990). Kriging and automated variogram modeling within a moving window. *Atmospheric Environment. Part A. General Topics* **24** 1759–1769.
- HAAS, T. C. (1995). Local Prediction of a Spatio-Temporal Process with an Application to Wet Sulfate Deposition. *Journal of the American Statistical Association* **90** 1189–1199.
- HALLIN, M., LU, Z. and TRAN, L. T. (2004). Local linear spatial regression. *The Annals of Statistics* **32** 2469–2500.
- JAYNE, S., ROEMMICH, D., ZILBERMAN, N., RISER, S., JOHNSON, K., JOHNSON, G. and PIOTROWICZ, S. (2017). The Argo Program: Present and Future. *Oceanography* **30** 18–28.
- KENNEDY, M. C. and O'HAGAN, A. (2001). Bayesian calibration of computer models. *Journal of the Royal Statistical Society: Series B (Statistical Methodology)* **63** 425–464.
- KUK, A. Y. C. (1995). Asymptotically Unbiased Estimation in Generalized Linear Models with Random Effects. *Journal of the Royal Statistical Society. Series B (Methodological)* **57** 395–407.
- KUUSELA, M. and STEIN, M. L. (2018a). Locally stationary spatio-temporal interpolation of Argo profiling float data. *Proceedings of the Royal Society A: Mathematical, Physical and Engineering Sciences* **474** 20180400.
- KUUSELA, M. and STEIN, M. L. (2018b). Supplementary material from "Locally stationary spatio-temporal interpolation of Argo profiling float data".
- LAGERLOEF, G. S. E., MITCHUM, G. T., LUKAS, R. and NIILER, P. P. (1999). Tropical Pacific Near-Surface Currents Estimated from Altimeter, Wind, and Drifter Data.
- LEBEDEV, K., YOSHINARI, H., MAXIMENKO, N. A. and HACKER, P. W. (2007). YoMaHa'07: Velocity data assessed from trajectories of Argo floats at parking level and at the sea surface. **4** 16.
- LIU, Y. and DE BRABANTER, K. (2018). Derivative Estimation in Random Design. In *Advances in Neural Information Processing Systems 31* (S. Bengio, H. Wallach, H. Larochelle, K. Grauman, N. Cesa-Bianchi and R. Garnett, eds.) 3445–3454. Curran Associates, Inc.
- MACDONALD, A. M. and BARINGER, M. (2013). Ocean Heat Transport. In *International Geophysics*, **103** 759–785.
- MCDUGALL, T. and BARKER, P. M. (2011). Getting started with TEOS-10 and the Gibbs Seawater (GSW) Oceanographic Toolbox. *SCOR/IAPSO WG* **127** 1–28.
- MCPHADEN, M. J., SANTOSO, A. and CAI, W. (2020). *El Niño Southern Oscillation in a Changing Climate*. American Geophysical Union (AGU).
- MERCHANT, C. J., EMBURY, O., BULGIN, C. E., BLOCK, T., CORLETT, G. K., FIEDLER, E., GOOD, S. A., MITTAZ, J., RAYNER, N. A., BERRY, D., EASTWOOD, S., TAYLOR, M., TSUSHIMA, Y., WATERFALL, A., WILSON, R. and DONLON, C. (2019). Satellite-based time-series of sea-surface temperature since 1981 for climate applications. *Scientific Data* **6** 223. Number: 1 Publisher: Nature Publishing Group.
- NEAL, R. M. and HINTON, G. E. (1998). A View of the Em Algorithm that Justifies Incremental, Sparse, and other Variants. In *Learning in Graphical Models*, (M. I. Jordan, ed.). *NATO ASI Series* 355–368. Springer Netherlands, Dordrecht.
- NOCEDAL, J. (1980). Updating quasi-Newton matrices with limited storage. *Mathematics of Computation* **35** 773–782.
- OLLITRAULT, M. and RANNOU, J.-P. (2013). ANDRO: An Argo-Based Deep Displacement Dataset. *Journal of Atmospheric and Oceanic Technology* **30** 759–788.
- PARK, B., KUUSELA, M., GIGLIO, D. and GRAY, A. (2020). Supplement to "Spatio-temporal Local Interpolation of Global Ocean Heat Transport using Argo Floats: A Debiased Latent Gaussian Process Approach".
- RASMUSSEN, C. E. and WILLIAMS, C. K. I. (2006). *Gaussian processes for machine learning*. MIT Press.
- REN, H.-L., WANG, R., ZHAI, P., DING, Y. and LU, B. (2017). Upper-ocean dynamical features and prediction of the super El Niño in 2015/16: A comparison with the cases in 1982/83 and 1997/98. *Journal of Meteorological Research* **31** 278–294.
- RIDGWAY, K. R., DUNN, J. R. and WILKIN, J. L. (2002). Ocean interpolation by four-dimensional weighted least squares - Application to the waters around Australasia. *Journal of Atmospheric and Oceanic Technology* **19** 1357–1375.
- RIO, M. H. and SANTOLERI, R. (2018). Improved global surface currents from the merging of altimetry and Sea Surface Temperature data. *Remote Sensing of Environment* **216** 770–785.
- RIO, M.-H., MULET, S., ETIENNE, H., PICOT, N. and DIBARBOURE, G. (2018). New CNES-CLS18 Mean Dynamic Topography of the global ocean from altimetry, gravity and in-situ data. In *OSTST* 22.
- RISER, S. C., FREELAND, H. J., ROEMMICH, D., WIJFFELS, S., TROISI, A., BELBÉOCH, M., GILBERT, D., XU, J., POULIQUEN, S., THRESHER, A., LE TRAON, P.-Y., MAZE, G., KLEIN, B., RAVICHANDRAN, M., GRANT, F., POULAIN, P.-M., SUGA, T., LIM, B., STERL, A., SUTTON, P., MORK, K.-A., VÉLEZ-BELCHÍ, P. J., ANSORGE, I., KING, B., TURTON, J., BARINGER, M. and JAYNE, S. R. (2016). Fifteen years of ocean observations with the global Argo array. *Nature Climate Change* **6** 145–153.
- ROEMMICH, D. and GILSON, J. (2009). The 2004–2008 mean and annual cycle of temperature, salinity, and steric height in the global ocean from the Argo Program. *Progress in Oceanography* **82** 81–100.

- ROEMMICH, D., BOEBEL, O., FREELAND, H. J., KING, B. A., LE TRAON, P.-Y., MOLINARI, R., OWENS, W. B., RISER, S., SEND, U., TAKEUCHI, K. and WIJFFELS, S. E. (1998). *On the design and implementation of Argo: A global array of profiling floats. ICPO publication series ; 21*. GODAE International Project Office, Melbourne, Vic.
- ROULSTON, M. S. and SMITH, L. A. (2002). Evaluating Probabilistic Forecasts Using Information Theory. *Monthly Weather Review* **130** 1653–1660.
- RUDNICK, D. L. (2016). Ocean Research Enabled by Underwater Gliders. *Annual Review of Marine Science* **8** 519–541.
- RUDNICK, D. L., DAVIS, R. E. and SHERMAN, J. T. (2016). Spray Underwater Glider Operations. *Journal of Atmospheric and Oceanic Technology* **33** 1113–1122.
- RUPPERT, D. and WAND, M. P. (1994). Multivariate Locally Weighted Least Squares Regression. *The Annals of Statistics* **22** 1346–1370. [MR1311979](#)
- SCOTT, R. B., ARBIC, B. K., CHASSIGNET, E. P., COWARD, A. C., MALTRUD, M., MERRYFIELD, W. J., SRINIVASAN, A. and VARGHESE, A. (2010). Total kinetic energy in four global eddying ocean circulation models and over 5000 current meter records. *Ocean Modelling* **32** 157–169.
- SHERMAN, J., DAVIS, R. E., OWENS, W. B. and VALDES, J. (2001). The autonomous underwater glider "Spray". *IEEE Journal of Oceanic Engineering* **26** 437–446.
- SIBSON, R. (1981). A brief description of natural neighbor interpolation. In *Interpolating multivariate data. Chapter 2* 21–36. John Wiley & Sons, New York.
- STEIN, M. L. (1999). *Interpolation of Spatial Data: Some Theory for Kriging. Springer Series in Statistics*. Springer-Verlag, New York.
- STEIN, M. L. (2013). Statistical Properties of Covariance Tapers. *Journal of Computational and Graphical Statistics* **22** 866–885.
- STEIN, M. L. (2019). Some Statistical Issues in Climate Science. 17.
- STOCKER, T. F. (2013). Chapter 1 - The Ocean as a Component of the Climate System. In *International Geophysics*, (G. Siedler, S. M. Griffies, J. Gould and J. A. Church, eds.). *Ocean Circulation and Climate* **103** 3–30. Academic Press.
- STONE, C. J. (1980). Optimal Rates of Convergence for Nonparametric Estimators. *Annals of Statistics* **8** 1348–1360. [MR594650](#)
- TABURET, G., SANCHEZ-ROMAN, A., BALLAROTTA, M., PUJOL, M.-I., LEGEAIS, J.-F., FOURNIER, F., FAUGERE, Y. and DIBARBOURE, G. (2019). DUACS DT2018: 25 years of reprocessed sea level altimetry products. *Ocean Science* **15** 1207–1224.
- TALLEY, L. D., PICKARD, G. L., EMERY, W. J. and SWIFT, J. H. (2011). *Descriptive Physical Oceanography: An Introduction*, 6 ed. Academic Press.
- TRENBERTH, K. E. and CARON, J. M. (2001). Estimates of Meridional Atmosphere and Ocean Heat Transports. *Journal of Climate* **14** 3433–3443.
- TRENBERTH, K. E. and SOLOMON, A. (1994). The global heat balance: heat transports in the atmosphere and ocean. *Climate Dynamics* **10** 107–134.
- TRENBERTH, K. E., FASULLO, J. T., SCHUCKMANN, K. v. and CHENG, L. (2016). Insights into Earth's Energy Imbalance from Multiple Sources. *Journal of Climate* **29** 7495–7505.
- VECCHIA, A. V. (1988). Estimation and Model Identification for Continuous Spatial Processes. *Journal of the Royal Statistical Society: Series B (Methodological)* **50** 297–312.
- VERDIÈRE, A. C. D., MEUNIER, T. and OLLITRAULT, M. (2019). Meridional overturning and heat transport from Argo floats displacements and the Planetary Geostrophic Method (PGM). Application to the subpolar North Atlantic. *Journal of Geophysical Research: Oceans* **0**.
- WANG, W. and LIN, L. (2015). Derivative estimation based on difference sequence via locally weighted least squares regression. *Journal of Machine Learning Research* **16** 2617–2641.
- WILLIS, J. K. and FU, L.-L. (2008). Combining altimeter and subsurface float data to estimate the time-averaged circulation in the upper ocean. *Journal of Geophysical Research: Oceans* **113**.
- WONG, A. P. S., WIJFFELS, S. E., RISER, S. C., POULIQUEN, S., HOSODA, S., ROEMMICH, D., GILSON, J., JOHNSON, G. C., MARTINI, K., MURPHY, D. J., SCANDERBEG, M., BHASKAR, T. V. S. U., BUCK, J. J. H., MERCEUR, F., CARVAL, T., MAZE, G., CABANES, C., ANDRÉ, X., POFFA, N., YASHAYAIEV, I., BARKER, P. M., GUINEHUT, S., BELBÉOCH, M., IGNASZEWSKI, M., BARINGER, M. O., SCHMID, C., LYMAN, J. M., MCTAGGART, K. E., PURKEY, S. G., ZILBERMAN, N., ALKIRE, M. B., SWIFT, D., OWENS, W. B., JAYNE, S. R., HERSH, C., ROBBINS, P., WEST-MACK, D., BAHR, F., YOSHIDA, S., SUTTON, P. J. H., CANCOUËT, R., COATANOAN, C., DOBBLER, D., JUAN, A. G., GOURRION, J., KOŁODZIEJCZYK, N., BERNARD, V., BOURLÈS, B., CLAUSTRE, H., D'ORTENZIO, F., LE RESTE, S., LE TRAON, P.-Y., RANNOU, J.-P., SAOUT-GRIT, C., SPEICH, S., THIERRY, V., VERBRUGGE, N., ANGEL-BENAVIDES, I. M., KLEIN, B., NOTARSTEFANO, G., POULAIN, P.-M., VÉLEZ-BELCHÍ, P., SUGA, T., ANDO, K., IWASASKA, N., KOBAYASHI, T., MASUDA, S., OKA, E., SATO, K.,

- NAKAMURA, T., SATO, K., TAKATSUKI, Y., YOSHIDA, T., COWLEY, R., LOVELL, J. L., OKE, P. R., VAN WIJK, E. M., CARSE, F., DONNELLY, M., GOULD, W. J., GOWERS, K., KING, B. A., LOCH, S. G., MOWAT, M., TURTON, J., RAMA RAO, E. P., RAVICHANDRAN, M., FREELAND, H. J., GABOURY, I., GILBERT, D., GREENAN, B. J. W., OUELLET, M., ROSS, T., TRAN, A., DONG, M., LIU, Z., XU, J., KANG, K., JO, H., KIM, S.-D. and PARK, H.-M. (2020). Argo Data 1999–2019: Two Million Temperature-Salinity Profiles and Subsurface Velocity Observations From a Global Array of Profiling Floats. *Frontiers in Marine Science* **7**. Publisher: Frontiers.
- YARGER, D., STOEV, S. and HSING, T. (2020). A functional-data approach to the Argo data. *arXiv:2006.05020 [stat]*. arXiv: 2006.05020.
- ZHENG, Y. and GIESE, B. S. (2009). Ocean heat transport in Simple Ocean Data Assimilation: Structure and mechanisms. *Journal of Geophysical Research: Oceans* **114**.

#### APPENDIX A: ALTERNATIVE DECOMPOSITION OF OHT

One may argue that heat transport can be computed by estimating mass transport and temperature grids separately. In particular,

$$(18) \quad Q = \int \theta M dz = \int (\bar{\theta} + \theta')(\bar{M} + M') dz, \quad M := \rho \mathbf{v}$$

Such a decomposition may identify which component—mean or anomaly—in temperature and mass transport drives heat transport. The decomposition does not need a two-step estimation procedure, rather it executes single step estimation for temperature and mass transport, separately. In Section 5, we empirically demonstrate that this strategy is inferior to the proposed two-stage method when it comes to prediction performance.

## SUPPLEMENTARY MATERIAL

**A. Quality Control.** On top of the quality control criteria applied in [Kuusela and Stein \(2018b\)](#), we additionally reject potential duplicates of each profile having the same spatial location with timestamps within 15 minutes since such duplicates are highly unlikely based on the Argo sampling design.

In general, salinity measurements are more prone larger biases than the temperature measurements by the nature of the CTD sensor and thus stricter quality control criteria are often required. We inspected the computed dynamic height anomalies and filtered out 34 profiles that were impacted by problematic salinity measurements. These profiles deviate more than  $3 \times$  interquartile range (IQR) from the median at 10 dbar and more than  $10 \times$  IQR at deeper depths.

**B. Analytic derivative of Matérn covariance kernel.** For our covariance kernel choice (7), we have the following analytic forms for the gradient and the Hessian of the kernel  $k$ :

$$(S1) \quad \frac{\partial}{\partial x_1} k(\mathbf{s}_1, \mathbf{s}_2) = -3\phi \frac{\Delta_x}{\xi_x^2} \exp(-\sqrt{3}d),$$

$$(S2) \quad \frac{\partial^2}{\partial x_1 \partial x_2} k(\mathbf{s}_1, \mathbf{s}_2) = \frac{3\phi}{\xi_x^2} \left( 1 - \frac{\sqrt{3}}{d} \left( \frac{\Delta_x}{\xi_x} \right)^2 \right) \exp(-\sqrt{3}d),$$

$$(S3) \quad \frac{\partial^2}{\partial x_1 \partial y_2} k(\mathbf{s}_1, \mathbf{s}_2) = -\frac{3\sqrt{3}\phi}{d} \frac{\Delta_x}{\xi_x^2} \frac{\Delta_y}{\xi_y^2} \exp(-\sqrt{3}d),$$

where  $\Delta_x = x_1 - x_2$  and  $\Delta_y = y_1 - y_2$ .

**C. Alternating Maximization view of the EM procedure.** One may ask how does the coordinate ascent algorithm proposed in the main text link to the EM algorithm. We follow the maximization-maximization viewpoint of the EM algorithm following [Neal and Hinton \(1998\)](#). A similar argument was also made in [Andresen and Spokoiny \(2016\)](#). Under our LGPR model, let  $\Upsilon$  be a set of observed values of the quantity of interest and let  $\mathbf{Z}$  be a set of unobserved latent data whose joint probability is parameterized using  $\Xi$ . The EM algorithm iteratively computes the following two steps, for  $l = 1, 2, \dots$ ,

**E-Step:** Compute a distribution  $\tilde{P}^{(l)}$  over the range of  $\mathbf{Z}$  such that  $\tilde{P}^{(l)} = P(\mathbf{Z} | \Upsilon; \Xi^{(l-1)})$ .

**M-Step:** Set  $\Xi^{(l)} = \operatorname{argmax}_{\Xi} \mathbb{E}_{\tilde{P}^{(l)}} [\log P(\Upsilon, \mathbf{Z}; \Xi)]$ .

When  $\mathbf{Z} = \operatorname{argmax}_{\mathbf{B}} P(\Upsilon; \mathbf{B}, \Xi)$  is considered,  $\tilde{P}^{(l)}$  is just a point mass at  $\mathbf{B}^{(l)}$ , where  $\mathbf{B}^{(l)} = \operatorname{argmax}_{\mathbf{B}} P(\Upsilon; \mathbf{B}, \Xi^{(l-1)})$ . Thus, the E-step is equivalent to finding the  $\mathbf{B}$  that maximizes the likelihood  $\mathcal{L}$  given the  $\Xi^{(l-1)}$  from the previous iteration. Similarly,  $\mathbb{E}_{\tilde{P}^{(l)}} [\log P(\Upsilon, \mathbf{Z}; \Xi)] = \log P(\Upsilon, \mathbf{B}^{(l)}; \Xi)$  which implies that the M-step is equivalent to finding the maximizer of the likelihood  $\mathcal{L}$  given the  $\mathbf{B}^{(l)}$  found in the previous E-step.

**D. Details of the Approximate EM procedure.** The M-step is performed with the residuals from the previous E-step as described in the paper. In the following, we derive the analytic solution of the E-step assuming that the temporal grid  $\mathcal{T}$  consists of center points of each month. A generalization to more complex grids is straightforward following the LGPR construction. The subscript  $i, j$  corresponds to year  $i$  and month  $j$ , i.e.,  $y_{i,j}$  is a set of observation in year  $i$  within month  $j$ . For every  $\mathbf{x}^* \in \mathcal{X}$ , denote  $\beta := \beta(\mathbf{x}^*)$  and  $\xi_j := \xi(\mathbf{x}^*, t_j^*)$ ,

where  $t_j^* \in \mathcal{T}$  is the center point of month  $j$ . Then,

$$\begin{aligned} \log \mathcal{L}(\boldsymbol{\beta}|\boldsymbol{\Xi}) &= \log(p(y_{1,1:3}); \boldsymbol{\xi}_2) + \sum_{j=4}^{12} \log p(y_{1,j}|y_{1:(j-1)}; \boldsymbol{\beta}, \boldsymbol{\xi}_2, \dots, \boldsymbol{\xi}_{j-1}) \\ &\quad + \sum_{i=2}^I \sum_{j=1}^{12} \log p(y_{i,j}|y_{1:i-1,1:12}, y_{i,1:(j-1)}; \boldsymbol{\beta}, \boldsymbol{\Xi}), \\ \log \tilde{\mathcal{L}}(\boldsymbol{\beta}|\boldsymbol{\Xi}) &= \log(p(y_{1,1:3}); \boldsymbol{\xi}_2) + \sum_{j=4}^{12} \log p(y_{1,j}|y_{(j-2):(j-1)}; \boldsymbol{\beta}, \boldsymbol{\xi}_{j-1}) \\ &\quad + \sum_{i=2}^I \left[ \log p(y_{i,1}|y_{i-1,11:12}; \boldsymbol{\beta}, \boldsymbol{\xi}_{12}) + \log p(y_{i,2}|y_{i-1,12}, y_{i,1}; \boldsymbol{\beta}, \boldsymbol{\xi}_1) \right. \\ &\quad \left. + \sum_{j=3}^{12} \log p(y_{i,j}|y_{i,1:(j-1)}; \boldsymbol{\beta}, \boldsymbol{\xi}_{j-1}) \right], \end{aligned}$$

where  $\tilde{\mathcal{L}}$  is the Vecchia approximated likelihood with 3-month temporal lag.

From hereafter, we show the result for the first year ( $i = 1$ ) and drop the subscript  $i$  for conciseness. The summand with all years still maintains the same maximizer form with the only difference in  $Q$  and  $C$  below.

$$\begin{aligned} \log \tilde{\mathcal{L}}_1(\boldsymbol{\beta}|\boldsymbol{\Xi}) &\approx \log p(y_{[1:3]}; \boldsymbol{\xi}_2) + \sum_{j=4}^{12} \log p(y_j|y_{(j-2):(j-1)}; \boldsymbol{\xi}_{j-1}), \quad (\text{Vecchia}) \\ &= \log \phi(y_{[1:3]}; \eta_{[1:3]} \boldsymbol{\beta}, K(\boldsymbol{\xi}_2)) \\ &\quad + \sum_{j=4}^{12} \log \phi(y_{[j-2:j]}; \eta_{[j-2:j]} \boldsymbol{\beta} + K_{j,-j} K_{-j,-j}^{-1} (y_{-j} - \eta_{-j}) \boldsymbol{\beta}, K_{jj} - K_{j,-j} K_{-j,-j}^{-1} K_{-j,j}) \\ &\quad \stackrel{(*)}{\propto} \boldsymbol{\beta}^\top \left[ \underbrace{\eta_{[3]}^\top K(\boldsymbol{\xi}_2)^{-1} \eta_{[3]} + \sum_{j=4}^{12} (\eta_j - K_{j,-j} K_{-j,-j}^{-1} \eta_{-j})^\top [K^{-1}]_{jj} (\eta_j - K_{j,-j} K_{-j,-j}^{-1} \eta_{-j})}_{:=Q} \right] \boldsymbol{\beta} \\ &\quad - 2 \left[ \underbrace{y_{[3]}^\top K(\boldsymbol{\xi}_2)^{-1} \eta_{[3]} + \sum_{j=4}^{12} (y_j - K_{j,-j} K_{-j,-j}^{-1} y_{-j})^\top [K^{-1}]_{jj} (\eta_j - K_{j,-j} K_{-j,-j}^{-1} \eta_{-j})}_{:=C} \right] \boldsymbol{\beta}, \end{aligned}$$

where  $\phi(y; \mu, \Sigma)$  is the pdf of multivariate Normal distribution with mean  $\mu$  and variance  $\Sigma$ ;  $K = K(\boldsymbol{\xi}_{j-1})$  is a covariance matrix constructed from the parameter  $\boldsymbol{\xi}_{j-1}$  and subscript  $-j$  corresponds to all indices except month  $j$ . (\*) follows from Woodbery matrix identity,

$$\begin{aligned} (K_{jj} - K_{j,-j} K_{-j,-j}^{-1} K_{-j,j})^{-1} &= K_{jj}^{-1} - K_{jj}^{-1} K_{j,-j} \left( K_{-j,-j} + K_{-j,j} K_{jj}^{-1} K_{j,-j} \right)^{-1} K_{-j,j} K_{jj}^{-1} \\ &= [K^{-1}]_{jj} \end{aligned}$$

Therefore, the maximizer is

$$\hat{\boldsymbol{\beta}} = Q^{-1} C.$$

**E. Predictive distribution for a single depth OHT.** From Equation (8), the predictive distribution of  $\hat{\mathbf{v}}(s_i) := \mathbf{v}(s_i) | \mathcal{D}$  for coordinates  $s_i \in \mathcal{S}_{\mathcal{D}} \cap \widetilde{\mathcal{W}}(s^*)$  is  $n_i$ -dimensional Gaussian with mean  $\bar{\mu}_{\nabla_{\mathbf{x}}}(s_i)$  and variance  $\bar{\Sigma}_{\nabla_{\mathbf{x}}}(s_i)$  as follows:

$$\begin{aligned} \bar{\mu}_{\nabla_{\mathbf{x}}}(s_i) &= \mu_{\mathbf{v}_{\text{ref}}}(s_i) + R \left[ \nabla_{\mathbf{x}} m_{\Psi}(s_i) + \nabla_{\mathbf{x}} k_{\Psi}(s_i, s_i) \widetilde{\mathbf{K}}_{\Psi, i}^{-1} [\Psi_i - m_{\Psi}(s_i)] \right] \\ \bar{\Sigma}_{\nabla_{\mathbf{x}}}(s_i) &= \Sigma_{\mathbf{v}_{\text{ref}}}(s_i) + R \left[ H_{\Psi}(s_i, s_i) - \nabla_{\mathbf{x}^*} k_{\Psi}(s_i, s_i)^{\top} \widetilde{\mathbf{K}}_{\Psi, i}^{-1} \nabla_{\mathbf{x}^*} k_{\Psi}(s_i, s_i) \right] R^{\top} \end{aligned}$$

where  $\mu_{\mathbf{v}_{\text{ref}}}$ ,  $\Sigma_{\mathbf{v}_{\text{ref}}}$  are the estimates and the mapping error from reference velocity estimates,  $H(s, s')$  is the Hessian of the kernel  $k(s, s')$  and  $\widetilde{\mathbf{K}}_{\Psi, i} = \mathbf{K}_{\Psi, i} + \hat{\sigma}_{\epsilon}^2 I_{n_i}$ .

Similarly, the predictive distribution of  $\text{OHT}(s^{**}) | \mathbf{v}(\mathcal{S}_{\mathcal{D}}), \mathcal{D}$  for any  $s^{**} \in \widetilde{\mathcal{W}}(s^*)$  is a Gaussian with mean  $\bar{\mu}_{\text{OHT} | \mathbf{v}}$  and variance  $\bar{\sigma}^2_{\text{OHT} | \mathbf{v}}$  where

$$\begin{aligned} \bar{\mu}_{\text{OHT} | \mathbf{v}}(s^{**}) &= m_{\text{OHT} | \mathbf{v}}(s^{**}) + k_{\text{OHT} | \mathbf{v}}(s^{**}, s_i) \widetilde{\mathbf{K}}_{\text{OHT} | \mathbf{v}, i}^{-1} [\theta_i \odot \mathbf{v}_i - m_{\text{OHT} | \mathbf{v}}(s_i)] \\ \bar{\sigma}^2_{\text{OHT} | \mathbf{v}}(s^{**}) &= k_{\text{OHT} | \mathbf{v}}(s^{**}, s^{**}) - k_{\text{OHT} | \mathbf{v}}(s^{**}, s_i)^{\top} \widetilde{\mathbf{K}}_{\text{OHT} | \mathbf{v}, i}^{-1} k_{\text{OHT} | \mathbf{v}}(s_i, s^{**}) \end{aligned}$$

where  $\theta_i := \theta(s_i)$  and  $\odot$  is a Hadamard product.

Since  $\text{OHT} | \mathbf{v}, \mathcal{D}$  and  $\mathbf{v} | \mathcal{D}$  forms a linear Gaussian system, the predictive distribution  $\text{OHT}_i(s^{**}) | \mathcal{D}$  at spatio-temporal coordinate  $s^{**}$  within  $\widetilde{\mathcal{W}}(s^*)$  is a Gaussian with mean  $\bar{\mu}_{\text{OHT}}$  and variance  $\bar{\sigma}^2_{\text{OHT}}$ .

$$\begin{aligned} \text{OHT}_i(s^{**}) | \mathcal{D} &\propto \mathcal{N}(\bar{\mu}_{\text{OHT} | \mathbf{v}}(s^{**}), \bar{\sigma}^2_{\text{OHT} | \mathbf{v}}(s^{**})) \cdot \mathcal{N}(\theta_i \odot \bar{\mu}_{\nabla_{\mathbf{x}}}(s_i), [\theta_i \theta_i^{\top}] \odot \bar{\Sigma}_{\nabla_{\mathbf{x}}}(s_i)) \\ &= \mathcal{N}(\bar{\mu}_{\text{OHT}}(s^{**}), \bar{\sigma}^2_{\text{OHT}}(s^{**})) \\ \bar{\mu}_{\text{OHT}}(s^{**}) &= m_{\text{OHT} | \mathbf{v}}(s^{**}) + k_{\text{OHT} | \mathbf{v}}(s^{**}, s_i) \widetilde{\mathbf{K}}_{\text{OHT} | \mathbf{v}, i}^{-1} [\theta_i \odot \bar{\mu}_{\nabla_{\mathbf{x}}}(s_i) - m_{\text{OHT} | \mathbf{v}}(s_i)] \\ \bar{\sigma}^2_{\text{OHT}}(s^{**}) &= k_{\text{OHT} | \mathbf{v}}(s^{**}, s_i) \widetilde{\mathbf{K}}_{\text{OHT} | \mathbf{v}, i}^{-1} [\theta_i \theta_i^{\top}] \odot \bar{\Sigma}_{\nabla_{\mathbf{x}}}(s_i) \widetilde{\mathbf{K}}_{\text{OHT} | \mathbf{v}, i}^{-1} k_{\text{OHT} | \mathbf{v}}(s_i, s^{**}) \\ &\quad + \bar{\sigma}^2_{\text{OHT} | \mathbf{v}}(s^{**}). \end{aligned}$$

## F. Upscaled surface satellite estimates.

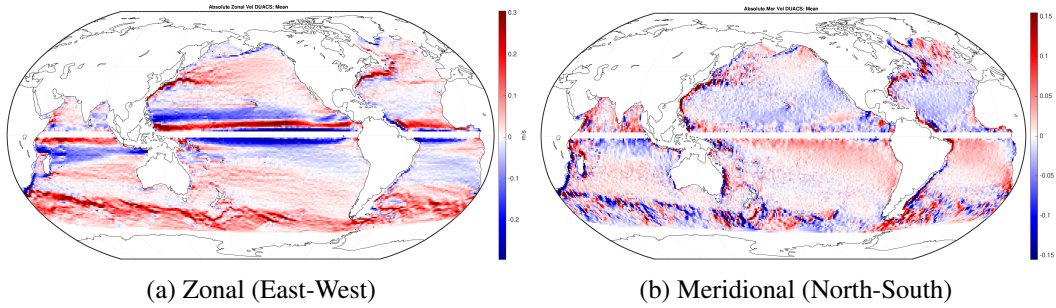


Fig S1: Upscaled time averaged surface velocity from satellite product (DUACS)

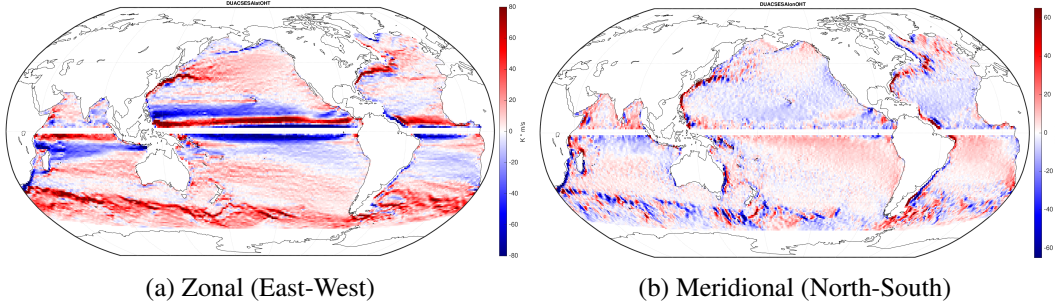


Fig S2: Upscaled time averaged surface temperature transport from satellite products (DUACS, CCI-C3S)

**G. Additional comparative numerical studies.** Given the pseudo-observations generated from the multimission satellite observations used in the validation study in Section 5, we compare the predicted monthly full field at every grid point in the global open ocean ( $\mathcal{X}$ ) during 2007–2018 ( $\mathcal{T}$ ) to the ground truth full fields, i.e., the upscaled absolute dynamic topography  $\Psi$ , velocity  $\mathbf{v}$ , and surface heat transport  $\text{TT}_0$  gridded fields (Figs. S1 and S2). We evaluate the predictive performance with two metrics: ignorance score (IGN, Roulston and Smith, 2002) and root mean squared error (RMSE). Let  $\Upsilon$  be either  $\Psi$ ,  $\mathbf{v}$ , or  $\text{TT}_0$ . Then,

$$\text{IGN} = - \sum_{s \in \mathcal{S}} \log p(\Upsilon_{\mathcal{T}}(s) \mid \mathcal{D}; \hat{\mathbf{B}}, \hat{\mathbf{\Xi}}), \quad \text{RMSE} = \sqrt{\frac{1}{|\mathcal{S}|} \sum_{s \in \mathcal{S}} \left( \Upsilon_{\mathcal{T}}(s) - \hat{\Upsilon}(s; \hat{\mathbf{B}}, \hat{\mathbf{\Xi}}) \right)^2},$$

where  $\Upsilon_{\mathcal{T}}(s)$  is the ground truth  $\Upsilon$  at  $s$ , and  $p(\cdot \mid \mathcal{D})$  is the predictive Gaussian density function. While RMSE measures the deterministic accuracy, IGN measures the probabilistic accuracy by assessing the goodness of fit of the predictive distribution learned from the data to the ground truth.

**G.1. Effect of window size.** We investigate how the spatial bandwidth choice  $\lambda_G$  affects the prediction of the velocity and  $\text{TT}_0$  fields. Figure S3 shows the predictive performance metrics of velocities for  $\lambda_G \in \{3^\circ, 4^\circ, 5^\circ\}$ . This result highlights the impact of  $\lambda_G$  to the predictive performance in the first stage of our procedure. A  $4^\circ$  spatial window is the optimal choice in minimizing RMSE of both zonal and meridional velocities and in minimizing IGN of zonal velocity. One could consider  $5^\circ$  if minimizing IGN of meridional velocity is the prime concern, but at the expense of worse zonal prediction performance and larger computational cost.

Figure S4 shows the predictive metrics of  $\text{TT}_0$  by  $\lambda_G$ . In computing the metrics, the same  $\lambda_G$  is used at both stages of the two-stage procedure. As it was the case for the velocities, a  $4^\circ$  spatial window is optimal for minimizing RMSE of both zonal and meridional  $\text{TT}_0$ . While IGN decreases as  $\lambda_G$  decreases, we do not choose the  $3^\circ$  window size since that choice leads to losing essential boundary dynamics due to too scarce data within the windows near the coastal boundaries. In conclusion, we adopt  $\lambda_G = 4^\circ$  for our main results in Sections 4 and 5.

**G.2. Approximate EM algorithm.** The goal of this analysis is to numerically investigate the claim that the proposed EM procedure improves over Kuusela and Stein (2018a) in both predictive performance and uncertainty quantification. Since the approximate EM procedure is agnostic to the quantity of interest, we focus on  $\Psi$  and  $\mathbf{v}$  in this comparison. This way,

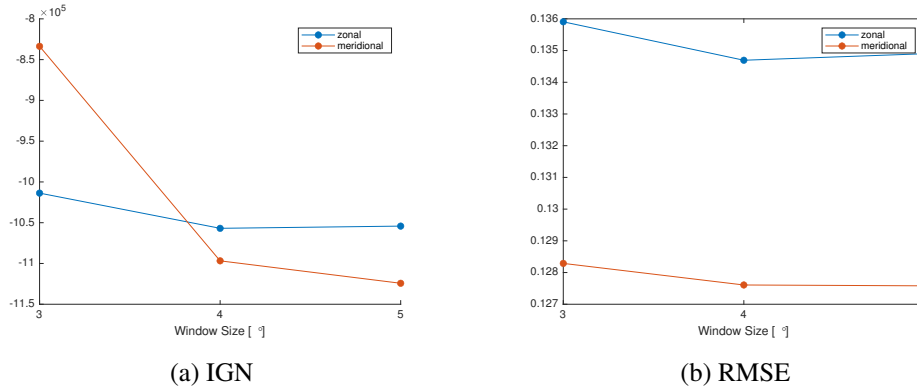


Fig S3: Performance metrics for predicting the velocity ( $\mathbf{v}$ ) field by varying window size.

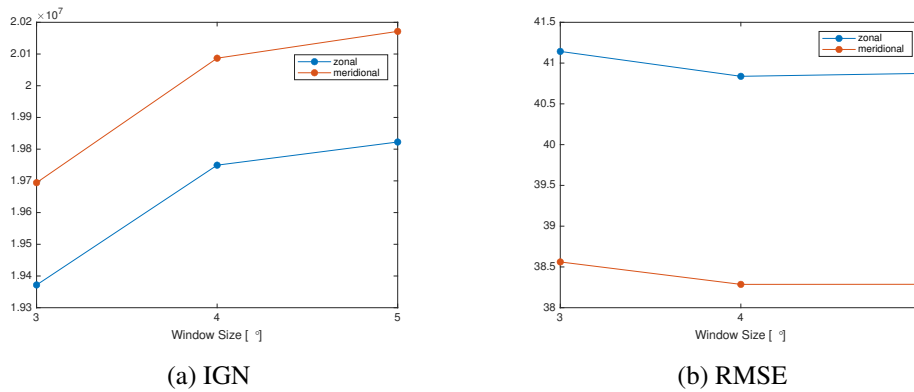


Fig S4: Performance metrics for predicting the  $TT_0$  field by varying window size.

we can compare the interpolation performance of the procedure to the ground truth  $\Psi$  field, as well as the prediction performance to the latent ground truth  $\mathbf{v}$ . Recall that [Kuusela and Stein \(2018a\)](#) use the [Roemmich and Gilson \(2009\)](#) mean field which is estimated by OLS and then estimate the covariance parameters from the residuals within the temporal window of interest. Even though the approximate EM procedure can aggregate the spatio-temporal covariance structure across different temporal windows in estimating the mean field, we limit the comparison to gridded full fields predicted at November 15th of every year, which is the center point of the temporal window for the local Gaussian process ranging from October 1st to December 31st, to make a fair comparison between the EM procedure and [Kuusela and Stein \(2018a\)](#).

Figures [S5](#) and [S6](#) show the predictive performance metrics—IGN and RMSE—of absolute dynamic topography and zonal and meridional velocities by EM iteration, respectively. Since iteration 0 corresponds to the performance of [Kuusela and Stein \(2018a\)](#), we conclude that jointly estimating the mean and the covariance parameters using the proposed EM procedure improves the predictive performance in both chosen metrics.

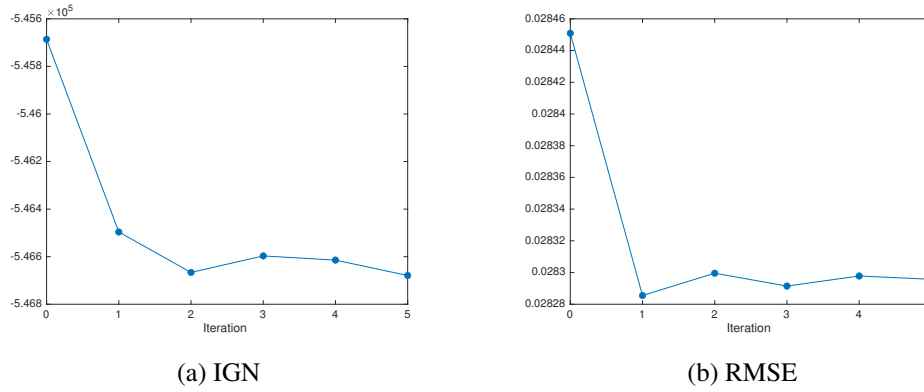


Fig S5: Performance metrics for predicting the absolute dynamic topography ( $\Psi$ ) field by EM iteration.

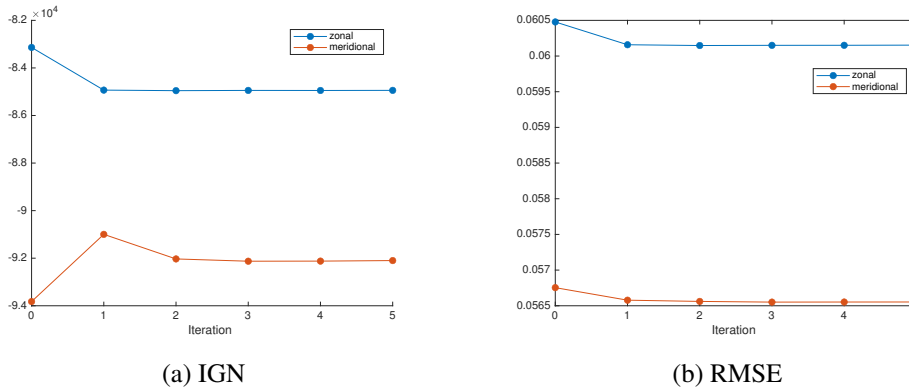
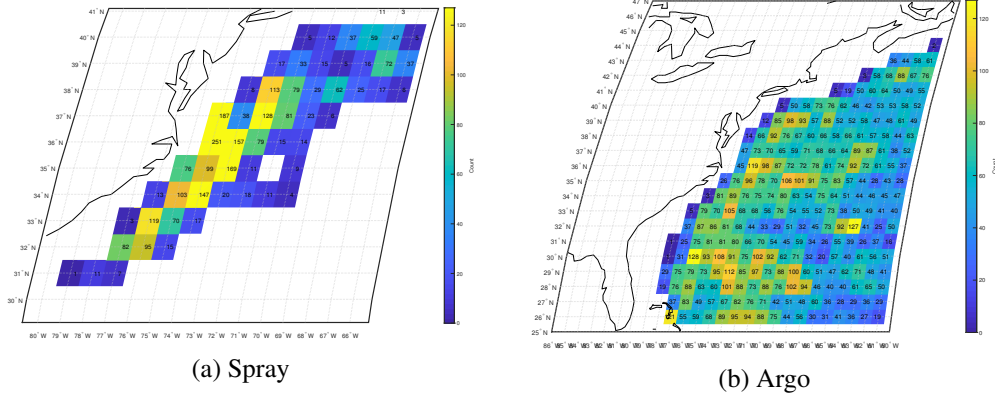


Fig S6: Performance metrics for predicting the velocity ( $\mathbf{v}$ ) field by EM iteration.

**H. Joint Analysis of Argo and Spray Gliders.** Spray underwater gliders (Sherman et al., 2001; Rudnick, Davis and Sherman, 2016) are buoyancy driven autonomous profiling vehicles that drive along strong fronts in a sawtooth path. With float density decreasing dramatically within the Gulf Stream on its shoreward side, the Argo program cannot (and is not intended to) thoroughly sample the Gulf Stream along the continental shelf, but gliders can ably fill this role (Todd and Locke-Wynn, 2017).

Similarly to the Argo program, Spray gliders measure (in-situ) temperature, salinity, and pressure. In addition, they also measure absolute velocity. Out of 10,577 available profiles recorded between January 2007 and December 2018 (Rudnick, Davis and Sherman, 2016), 2,791 (26.4%) profiles have measurements down to 900 dbar. These profiles can be used along with the Argo profiles to improve the geostrophic velocity estimate. Figure S7 shows the number of profiles binned in  $1^\circ \times 1^\circ$  grid at 15 dbar from Spray and Argo, respectively.

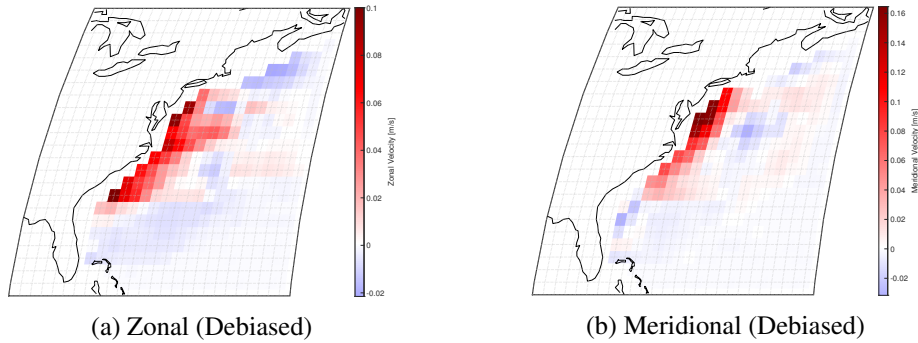
Argo-based estimates are in a surprisingly good agreement with satellite estimates as we may see from the validation section in the main paper. Most regions with relatively larger residuals, however, are close to the continental shelves where Argo float density decreases dramatically within the shallow coastal region since the floats cannot dive to 2000 dbar. This decreased sampling density degrades the quality of the estimates. We empirically show that this is indeed the case by coalescing the Spray glider observations with the Argo array. Under our data-driven statistical framework, we can simply form the union of the two data sets and


 Fig S7: Number of profiles in  $1^\circ \times 1^\circ$  grid at 15dbar.

re-run the mapping algorithms with the combined set of data. We re-estimate all the relevant coefficients, covariance parameters, and apply the debiasing procedure to the aggregated data.

**H.1. Geostrophic Velocity  $\hat{v}$ .** Figure S8 illustrates the difference in the time averaged mean geostrophic velocity  $A_v(\hat{v})$  at 15 dbar between estimates from aggregated Argo and Spray profiles and from Argo profiles only. Positive value in red means that the estimate from the aggregated data has a larger value than that from Argo by itself. While the magnitude difference is smaller in deeper depth, the qualitative differences in deeper depths were consistent with Figure S8.

Clearly, including the Spray gliders helps resolve underestimated signals close to coastal shelves. The improvement is not only substantial in magnitude but also has a critical impact for quantifying ocean heat transport, in that WBCs are the key driving component in the large-scale ocean circulation. This also implies that the miscalibration near the coastal shelves is due to an innate limitation in the spatial coverage of the Argo array rather than due to insufficient statistical modeling.


 Fig S8: Time averaged Mean velocity  $A_v(\hat{v})$  differences at 15dbar.

**H.2. Heat Transport  $\hat{OHT}$  and  $MHT$ .** The Argo-only underestimate in the geostrophic velocity  $\hat{v}$  has a direct consequence on the heat transport. Figure S9 illustrates the difference in the upper ocean time averaged mean heat transport  $A_v(\hat{OHT})$  between estimates from the aggregated profiles and those from Argo profiles only. Positive values in red mean that there

is more transport when Spray profiles were included in the analysis. The result shown is based on the seasonally averaged mean transport suppressing the seasonal cycle explicitly modeled for OHT. Similar spatial underestimation near the coastal shelves for both  $\widehat{\text{Av}}(\widehat{\text{OHT}})$  and  $\widehat{\text{Av}}(\widehat{v})$  confirms that the velocity underestimation was consistent throughout varying depths.

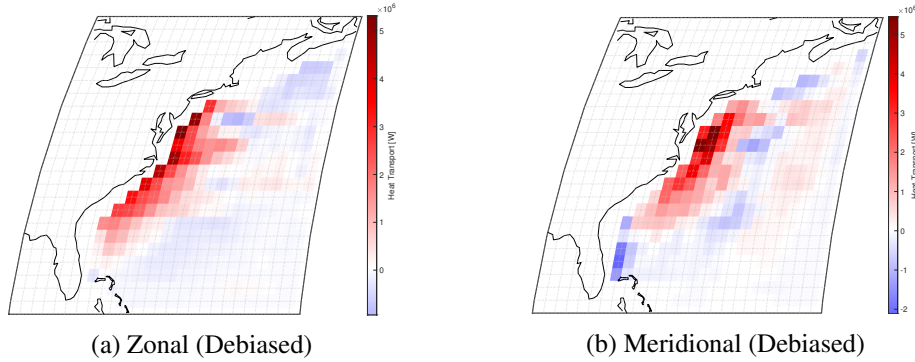


Fig S9: Mean absolute heat transport  $\widehat{\text{Av}}(\widehat{\text{OHT}})$  differences over 10 to 900 dbar.

Mean meridional heat transport (MHT) differences in Figure S10 summarize the aggregated underestimated signals over the relevant latitudes. Positive difference implies that there is more transport when Spray profiles were jointly analyzed with Argo. The black bold line corresponds to the seasonally averaged transport as shown in Figure S9 and separate monthly transports accounting for the seasonal cycle are overlaid. There is a large fluctuation between  $28^\circ\text{N}$  to  $32^\circ\text{N}$  in early and late summer months. Nevertheless, the Spray gliders effectively capture the underestimated heat transport in general.

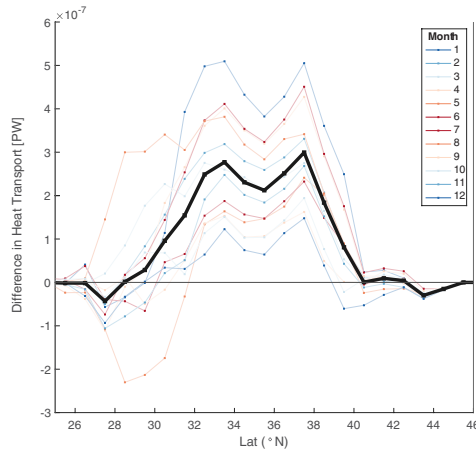


Fig S10: Estimated difference in mean Meridional Heat Transport from 10 dbar to 900 dbar.

## REFERENCES

ANDRESEN, A. and SPOKOINY, V. (2016). Convergence of an Alternating Maximization Procedure. *Journal of Machine Learning Research* **17** 1–53.

- KUUSELA, M. and STEIN, M. L. (2018a). Supplementary material from "Locally stationary spatio-temporal interpolation of Argo profiling float data".
- KUUSELA, M. and STEIN, M. L. (2018b). Locally stationary spatio-temporal interpolation of Argo profiling float data. *Proceedings of the Royal Society A: Mathematical, Physical and Engineering Sciences* **474** 20180400.
- NEAL, R. M. and HINTON, G. E. (1998). A View of the Em Algorithm that Justifies Incremental, Sparse, and other Variants. In *Learning in Graphical Models*, (M. I. Jordan, ed.). *NATO ASI Series* 355–368. Springer Netherlands, Dordrecht.
- ROEMMICH, D. and GILSON, J. (2009). The 2004–2008 mean and annual cycle of temperature, salinity, and steric height in the global ocean from the Argo Program. *Progress in Oceanography* **82** 81–100.
- ROULSTON, M. S. and SMITH, L. A. (2002). Evaluating Probabilistic Forecasts Using Information Theory. *Monthly Weather Review* **130** 1653–1660.
- RUDNICK, D. L., DAVIS, R. E. and SHERMAN, J. T. (2016). Spray Underwater Glider Operations. *Journal of Atmospheric and Oceanic Technology* **33** 1113–1122.
- SHERMAN, J., DAVIS, R. E., OWENS, W. B. and VALDES, J. (2001). The autonomous underwater glider "Spray". *IEEE Journal of Oceanic Engineering* **26** 437–446.
- TODD, R. E. and LOCKE-WYNN, L. (2017). Underwater Glider Observations and the Representation of Western Boundary Currents in Numerical Models. *Oceanography* **30** 88–89.